MOX-Report No. 15/2024

Modeling and simulation of electrochemical and surface diffusion effects in filamentary cation-based resistive memory devices

Vaccaro, F.; Mauri, A.G.; Perotto, S.; Brivio, S.; Spiga, S.

MOX, Dipartimento di Matematica
Politecnico di Milano, Via Bonardi 9 - 20133 Milano (Italy)

mox-dmat@polimi.it https://mox.polimi.it

Modeling and simulation of electrochemical and surface diffusion effects in filamentary cation-based resistive memory devices

F. Vaccaro[#], A.G. Mauri[#], S. Perotto[#], S. Brivio[†], S. Spiga[†]

February 9, 2024

[#] MOX – Dipartimento di Matematica, Politecnico di Milano
Piazza L. da Vinci 32, I-20133 Milano, Italy
{francesco.vaccaro,aurelio.mauri,simona.perotto}@polimi.it

[†] CNR - IMM, Unità di Agrate Brianza
Via C. Olivetti 2, Agrate Brianza (MB), Italy
{stefano.brivio,sabina.spiga}@mdm.imm.cnr.it

Abstract

Cation-based (or electrochemical) resistive memory devices are gaining increasing interest in neuromorphic applications due to their capability to emulate the dynamic behaviour of biological neurons and synapses. The utilization of such devices in neuromorphic systems necessitates a reliable physical model for the resistance switching mechanism, which is based on the formation and dissolution of a conductive filament in a thin dielectric layer, sandwiched between two metal electrodes. We propose a comprehensive model to simulate the evolution of the filament geometry under the effect of both surface diffusion caused by curvature gradient and electromechanical stress, and mass injection due to electrodeposition of cations. The model has been implemented in a C++ platform using a level-set approach based on a mixed finite element formulation, enriched by a mesh adaptation strategy to accurately and efficiently track the evolution of the filament shape. The numerical scheme is initially validated on various benchmark case studies. We then simulate the growth and self-dissolution of the filamentary geometry, incorporating an electrical model allowing a comparison with conventional cation-based memories. The simulations showcase filament formation under varying applied voltages and filament dissolution under different initial resistances.

Keywords: RRAM memristive devices; resistive switching memory device; electrochemical metallization; level-set method; anisotropic adapted mesh; finite elements.

1 Introduction

Resistive random access memories (RRAMs) constitute an emerging class of memory technologies that has been widely investigated over the last 20 years [59, 13, 5]. RRAMs

are two-terminal devices capable of altering their resistance between at least two values. This characteristic has made them particularly attractive for neuromorphic computing architectures. Specifically, certain dynamic aspects of synapses and neurons have recently been replicated by cation-based RRAMs [62, 49, 57]. This advancement has propelled the realization of artificial brain-inspired chips closer to reality.
Cation-based RRAMs fall under the broader category of memristors, also referred to in the literature as electrochemical metallization cells, programmable metallization cells, or conductive bridge memories [59, 51, 18]. Cation-based RRAMs are structured with a metal/ionic conductor/metal configuration, where one electrode remains chemically inert (e.g., Pt, TiN), while the other is composed of electrochemically active species (e.g., Ag or Cu), as illustrated in Fig. 1. The ionic conductor is typically dielectric, such as oxides like HfO_2, ZrO_2, and SiO_2, as considered in [59, 32, 61]. A cation-based RRAM undergoes a transition from a very high to a low resistance state, through a series of electric field-activated processes [32, 59, 51, 57, 58, 61]. When a positive voltage is applied to the active electrode, cations are generated through the oxidation of the electrode atoms and are then injected into the dielectric (represented by the transformation from a green ball to a blue circle in Fig. 1a). These charged species undergo electric field-induced drift towards the inert electrode (illustrated by blue dashed circles in Fig. 1a) and ultimately deposit through reduction (from dashed blue circles to a purple ball in Fig. 1a) on the interface with the opposite electrode, leading to the formation of a metallic conductive filament (CF). The process continues until the CF shorts the two electrodes or leaves a small tunneling gap towards the active electrode, resulting in a low resistance state, as depicted in Fig. 1b). In Fig. 1c), a representative experimental current response of an Ag/SiO_x/Pt device is shown when a positive voltage is applied (indicated by the red voltage pulse in the inset). An abrupt transition occurs within a specific delay time ($\approx 2{\cdot}10^{-5}$ s). It's worth noting that we intentionally overlook the CF nucleation process, which may be significant under certain experimental conditions [32].

In volatile cation-based devices, the formed metallic CF becomes unstable due to excess energy accumulated at the CF/dielectric interface [4, 10]. This excess energy is reduced through interface area minimization, leading to CF dissolution, electrical disconnection of the top and bottom electrodes, and ultimately the restoration of a high resistance state. Unlike CF formation, its dissolution is a spontaneous process not driven by an electric field [56, 11, 12, 57]. The physical process can be described in terms of surface (specifically, interface) diffusion of atoms driven by curvature gradient [56], as illustrated in Fig. 1d)-e). In Fig. 1f), a representative evolution of the device current during spontaneous relaxation is depicted when a small non-perturbing voltage (indicated by the blue box in the inset) is applied. The transition from low to high resistance occurs within a specific relaxation time ($\approx 10^{-4}$ s in the reported case) after the programming voltage is released.

While there is a generally accepted understanding of the cation-based devices, a physics-based mathematical tool for simulating the device's operation in both CF growth and dissolution is only partially available in the literature. The processes of CF growth and retraction are well-described, including their temporal progression, by accurate com-

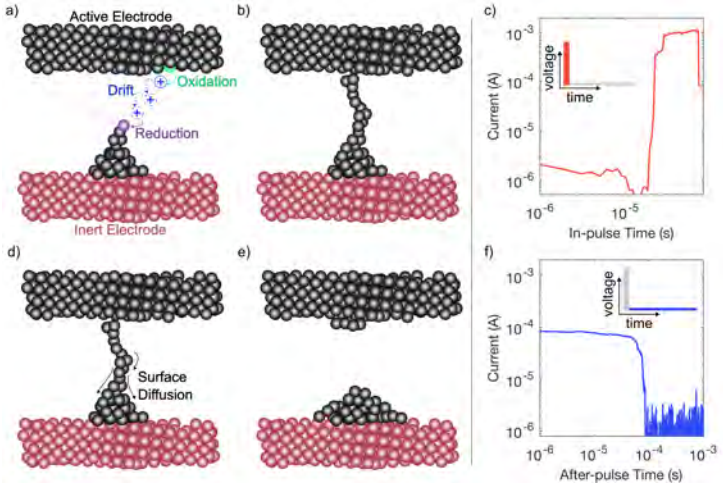

Figure 1: Growth of a CF driven by the oxidation of atoms at the active electrode, followed by cation drift and dissolution at the opposite interface (a). Formation of a connection between the active and inert electrodes (b). Representative current evolution of a Ag/SiO_x/Pt device when a 0.8 V - programming voltage is applied (c). Spontaneous rearrangement of the CF due to surface diffusion (d), leading to CF disconnection (e). Representative current evolution of a Ag/SiO_x/Pt device during self-CF-dissolution when a 0.05 V - non perturbing voltage is applied (f).

pact models. However, these models often do not account for CF geometry [32, 11, 55, 54]. The morphology of the CF, specifically during its growth, is considered in continuum [9, 18, 26] or Monte Carlo models [30, 16, 23, 41], whereas limited work is available on simulating only the CF dissolution [56].

The novelty of this study lies in the introduction within a finite element (FE) framework of electric field-activated processes in nanoscale geometries, incorporating surface diffusion driven by curvature gradients. We reframe the model presented in [56] into a level-set formulation, enabling the incorporation of the electric field-assisted evolution of the CF morphology. Notably, a level-set formulation applied to cation-based devices is sparsely documented in the literature [31, 18]. Additionally, given that the typical size of the CF is much smaller than the device dimension, we incorporate a tailored mesh adaptation strategy which ensures accurate solutions of the mathematical model within a reasonable computational time. The simulations reproduce the processes of CF growth and self-dissolution in agreement with the general interpretation of the operation principles of cation-based RRAMs. Furthermore, with the help of a simple electrical conduction model, the simulations also qualitatively reproduce the expected resistance evolution of formation and dissolution experiments.

The paper is structured as follows. In Sec. 2, we delve into the physical model adopted to describe the formation and dissolution of the CF, encompassing the effects of surface diffusion and the electric field. Section 3 focuses on the level-set approach, highlighting how it allows tracking the geometric evolution of the CF. The mathematical formulation

is summarized in Sec. 4, accompanied by the corresponding Galerkin approximation based on a mixed FE discretization. Mesh adaptation takes center stage in Sec. 5, leveraging an a posteriori anisotropic error estimator for the gradient of the level-set function. Section 6 outlines the entire computational workflow. In Sec. 7, we present results from various benchmark tests to illustrate the reliability of the proposed model. Section 8 applies the modeling framework to simulate filament formation and dissolution in a cation-based RRAM, including comparisons with typical electrical trends. Finally, Sec. 9 draws conclusions and offers perspectives on potential future developments.

2 The physical model

We introduce the physical model employed to simulate the evolution of a conductive filament (CF) in cation-based Resistive Random Access Memories (RRAMs). The first section details the impact of surface diffusion assisted by the electric field, while the second section enhances the model by incorporating electro-chemical deposition.

2.1 Morphological change of a conductor in an electric field

According to [39, 2, 44], the filament conductor surface tends to minimize the potential, $\mu = \mu(K)$, associated with the filament curvature K, being

$$\mu = \gamma_s \Omega_A K, \tag{1}$$

with γ_s the surface free energy per unit area and Ω_A the atomic volume.
The inclusion of the electric field $\boldsymbol{E}$ in this framework requires an important generalization. To this aim, the most straightforward way to proceed is to consider the variation per atom of a generalized potential, $\mu = \mu(K, E_n)$, under the effect of the surface curvature and of the electric field normal to the surface of the CF, $E_n = \boldsymbol{E} \cdot \boldsymbol{n}$, with $\boldsymbol{n}$ the unit outward normal vector to the conductor surface, S_g (see Fig. 2 for a sketch). Thus, the generalized potential energy can be expressed by

$$\mu = \gamma_s \Omega_A K + \frac{1}{2} \varepsilon \, \Omega_A E_n^2, \tag{2}$$

with ε the dielectric constant of the material, where the second term accounts for the normal component of the Maxwell stress produced by the electric field [33]. The gradient of μ along the surface induces a movement of atoms along the conductor surface, with an average velocity given by

$$\mathbf{v} = -\frac{D_s}{kT} \nabla_s \mu = -\frac{D_s \Omega_A}{kT} (\gamma_s \nabla_s K + \frac{1}{2} \varepsilon \nabla_s E_n^2), \tag{3}$$

after assuming valid the Nernst-Einstein relation [24], where D_s is the surface diffusion coefficient, k represents the Boltzmann constant, T is the temperature which is assumed constant, and

$$\nabla_s u = \nabla u - (\nabla u \cdot \boldsymbol{n}) \boldsymbol{n}, \tag{4}$$

denotes the surface gradient of a generic scalar function u, namely the tangential component of the gradient.

The flux of atoms, $\mathbf{J}_s$, along the metal surface (see Fig. 2) coincides with the product

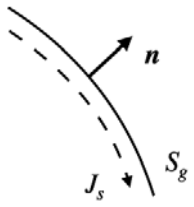

Figure 2: Sketch of the conductor surface, S_g, of the associated unit outward normal vector, $\boldsymbol{n}$, and of the surface flux, J_s.

of the average surface velocity, $\mathbf{v}$, by the number of atoms per unit area, ν_s, being

$$\mathbf{J}_s = -\frac{D_s \Omega_A \nu_s}{kT}(\gamma_s \nabla_s K + \frac{1}{2}\varepsilon \nabla_s E_n^2). \tag{5}$$

Following [39], we can calculate the modulus v_{n0} of the normal velocity, $\mathbf{v_{n0}} = v_{n0}\mathbf{n}$, to the surface element by multiplying the divergence of $-J_s$ by Ω_A, being

$$v_{n0} = \Omega_A \nabla \cdot \big(-\mathbf{J}_s\big) = \frac{D_s \Omega_A^2 \nu_s}{kT}(\gamma_s \nabla \cdot \nabla_s K + \frac{1}{2}\varepsilon \nabla \cdot \nabla_s E_n^2) \tag{6}$$

(for a more formal derivation, we refer the interested reader to [7, 6]). Notice that definition (6) holds in a neighborhood of S_g, due to the local feature of the surface current $\mathbf{J}_s$. Now, we rewrite (6) in a compact form by introducing the quantities

$$C_s = \frac{D_s \Omega_A^2 \nu_s \gamma_s}{kT}, \quad C_{el} = \frac{D_s \Omega_A^2 \nu_s \varepsilon}{2kT}$$

and the surface Laplacian (or Laplace-Beltrami) operator, $\nabla_s^2 = \nabla \cdot \nabla_s$, thus obtaining

$$v_{n0} = \left(C_s \nabla_s^2 K + C_{el} \nabla_s^2 E_n^2\right). \tag{7}$$

Relation (7) encompasses surface diffusion due to the curvature gradient and the electromechanical stress. In the next section, the definition of $\mathbf{v_{n0}}$ will be enriched by a reaction term in order to model the metal atom electro-deposition.

We observe that the evaluation of the normal electric field, E_n, in the equations above requires the solution of the generalized Poisson equation,

$$\begin{cases} \varepsilon_0 \nabla \cdot (-\varepsilon_r \nabla \varphi) = q \sum_{\alpha=1}^{M_{ion}} z_\alpha n_\alpha & \text{in} \quad \Omega_{dielectric} \\ \nabla \cdot (-\sigma \nabla \varphi) = \nabla \cdot (\sigma \nabla \alpha_T T) & \text{in} \quad \Omega_{metal}, \end{cases} \tag{8}$$

which models the electrostatic potential, φ, being $\boldsymbol{E} = -\nabla\varphi$ in $\Omega = \Omega_{dielectric} \cup \Omega_{metal}$, with $\Omega_{dielectric}$ and Ω_{metal} the dielectric and the metallic part of the simulation domain Ω,

respectively, and where $\varepsilon_0 = 8.85410^{-14}$ F/cm is the absolute permittivity (in vacuum), ε_r is the relative permittivity, q is the elementary charge, M_{ion} denotes the ion species in the device, z_α and n_α are the ionic charge and the number density of the species α, σ is the electrical conductivity and α_T represents the thermal conductivity [28]. Appropriate boundary conditions complete (8), to describe the polarization of the simulation domain (we refer to Sec. 8 for more details).

2.2 Metal atom deposition on the conductor surface

Growing a CF in a cation-based RRAM involves moving material from the active electrode to the inert electrode (or the growing CF). This occurs through a sequence of electric-field-driven processes, including atom oxidation, ionic drift, and ionic reduction. The dominant process among these depends on the applied device voltage [32]. In the current model, we assume that cation drift in the dielectric layer is significantly faster than the rates of oxidation and reduction at the metal/dielectric interfaces. This is equivalent to assuming that only the redox processes predominantly drive CF growth.

To model the metal atom deposition on the conductor surface, we have to modify the definition of the normal velocity by including an additional contribution which takes into account the inflow (outflow) of ionized atoms from the dielectric (the metal bulk) through the conductor surface, so that we define $\mathbf{v_n} = v_n\mathbf{n} = \mathbf{v_{n0}} + F(E_n)\mathbf{n}$ with

$$v_n = C_s\nabla_s^2 K + C_{el}\nabla_s^2 E_n^2 + F(E_n). \tag{9}$$

Definition (9) is limited to a neighborhood of the conductor surface, analogously to (7). In the redox-dominated regime, we can define the term $F(E_n)$ in (9) as the velocity of the oxidation/reduction process. In particular, we have

$$F(E_n) = v_r \exp\left(-\frac{\Delta E_{ox,r} - \gamma E_n}{kT}\right) = C_r \exp\left(\frac{\gamma E_n}{kT}\right), \tag{10}$$

with $C_r = v_r \exp\left(-\frac{\Delta E_{ox,r}}{kT}\right)$, where v_r denotes the reaction velocity, $\Delta E_{ox,r}$ is the activation energy, and where we account for the effect of the normal electric field as a reduction of the reaction barrier process through coefficient γ.
We highlight that equation (9) ultimately involves all the physical quantities characterizing the modeling of interest for the paper. In particular, the morphological change of a metallic inclusion in a dielectric under the effect of the surface atom diffusion, together with the electric field (i.e., electromechanical stress and chemical reactions) are now taken into account by the normal velocity, $\mathbf{v_n}$, of each local element along the metal surface. This modeling choice will be exemplified in Sec. 7.
Finally, in order to track the growth and dissolution of the metallic CF, we have to introduce a law which models the evolution of the conductor surface S_g (i.e., of a one-dimensional (1D) manifold in a two-dimensional (2D) framework, defining the shape of the CF in the device), so that $S_g = S_g(t)$. This goal will be reached by resorting to a level-set formulation, as detailed in the next section.

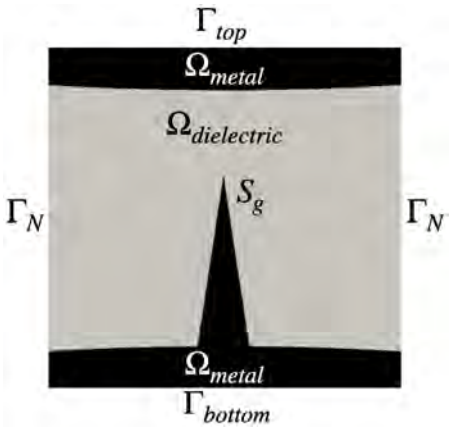

Figure 3: Sketch of typical cation-based RRAM device: Ω_{metal} and $\Omega_{dielectric}$ constitute the computational domain; Γ_{top}, Γ_{bottom} and Γ_N the associated boundary portions, with S_g the metal/dielectric interface.

3 Evolution of the conductor surface: a level-set formulation

We describe the temporal evolution of the CF in a cation-based RRAMs by resorting to the level-set method [40, 47, 46]. This approach allows describing, in a reliable and computationally efficient way, evolving curves and surfaces, that change morphology with time. The level-set method identifies the surface to be tracked with the zero level of a higher dimensional function. This approach has been successfully applied in several application contexts (see, e.g., [52, 3, 8]). Below, we detail, for completeness, the main steps of the adopted level-set approach, as it is preparatory to set the model proposed in Sec. 4 to describe the evolution of the CF.

Due to the model's complexity and the computational expense of a 3D domain, we opted for a 2D domain by cutting the CF with a plane normal to the electrode in the center, while avoiding any a-priori pre-established symmetry. Specifically, the domain, Ω, for the simulation of the CF evolution in a RRAM device consists of a metallic section (i.e., the electrodes and the CF), Ω_{metal}, and a dielectric part, $\Omega_{dielectric}$, so that $\overline{\Omega} = \overline{\Omega}_{dielectric} \cup \overline{\Omega}_{metal}$, with $S_g = \overline{\Omega}_{dielectric} \cap \overline{\Omega}_{metal}$ being the curve describing the CF shape (see Fig. 3 for a sketch). The evolution of the CF makes the subdomains $\Omega_{dielectric}$ and Ω_{metal} varying in time.
Concerning the domain boundary $\partial\Omega$ of Ω, we discriminate the contact region $\Gamma_{contact} = \Gamma_{top} \cup \Gamma_{bottom}$, where the bias to the device is applied, and the device floating portion, Γ_N, where no direct bias is enforced (see Fig. 3).

The level-set method consists in defining S_g as the level zero of a sufficiently smooth function, $\phi : \Omega \times \mathbb{R}^+ \to \mathbb{R}$, varying in time, i.e.,

$$S_g(t) = \big\{\mathbf{x} \in \Omega \,:\, \phi(\mathbf{x}, t) = 0\big\}. \tag{11}$$

The evolution in time of the level-set function is driven by the velocity $\mathbf{v_n}$, after extending definition (9) from a neighborhood of S_g to the whole domain Ω. Thus, the function ϕ coincides with the solution to the partial differential equation (PDE)

$$\frac{\partial \phi}{\partial t} + \mathbf{v_n} \cdot \nabla \phi = 0 \quad \text{in } \Omega. \tag{12}$$

In more detail, at time $t = 0$, the function ϕ can be assumed to coincide with a function h of the signed distance function, $d = d(\mathbf{x})$, in a neighbourhood of S_g of amplitude δ, namely,

$$\phi(\mathbf{x}, 0) = \phi_0(\mathbf{x}) = h(d(\mathbf{x})) \quad \text{with} \quad |d(\mathbf{x})| \leq \delta, \tag{13}$$

while taking positive and negative values outside and inside the region delimited by S_g, respectively. Following [7, 6], we choose

$$h(d(\mathbf{x})) = \frac{2\delta}{\pi} \sin\left(\frac{\pi d(\mathbf{x})}{2\delta}\right). \tag{14}$$

Then, we extend ϕ_0 to the whole domain Ω by setting $\phi_0(\mathbf{x}) = 2\delta/\pi$ for $d(\mathbf{x}) > \delta$ (i.e., outside S_g) and $\phi_0(\mathbf{x}) = -2\delta/\pi$ for $d(\mathbf{x}) < -\delta$ (i.e., inside S_g). This definition ensures ϕ_0 to be differentiable across the boundaries of the narrow band around S_g. The computation of the distance function $d(\mathbf{x})$, in general, is not a trivial task due to the generic shape CF may take. To this aim, we can resort, for instance, to a standard minimization of the distance between a given point external to S_g and any point internal to S_g. In such a case, the assignment of the sign to the distance is straightforward. As an alternative to the distance minimization, we can adopt the heat approach. This method exploits a classical geometric result, relating heat diffusion with geodesic distance, so that the distance is computed along shortest curves through the domain [15]. In such a context, the assignment of the sign is less trivial.
In the numerical assessment below, we adopt one approach rather than the other, depending on the application at hand.

Finally, we exploit the function ϕ to compute the normal direction, $\boldsymbol{n}$, to the surface S_g and the mean curvature, K, of the surface involved in the definition of the advective field $\mathbf{v_n}$. In particular, following [47, 40], we define

$$\mathbf{n} = \frac{\nabla \phi}{||\nabla \phi||} \tag{15}$$

and

$$K = \nabla \cdot \frac{\nabla \phi}{||\nabla \phi||}, \tag{16}$$

with $\|\cdot\|$ the $L^2(\Omega)$-norm, standard notation being used for function spaces [19]. Notice that definitions (15) and (16) generalize to the whole domain Ω through problem (12)-(14).

4 A new model model for the CF evolution

In this section, we formalize the PDE model proposed to describe the evolution of the CF geometry in a cation-based RRAM device due to surface diffusion and redox reactions. Successively, we adopt a finite element discretization to approximate the problem.

4.1 The PDE system

The complete system of equations modeling the CF evolution gathers the level-set equation (12) together with the generalized Poisson equations in (8), namely, we look for ϕ and φ such that

$$\begin{cases} \dfrac{\partial \phi}{\partial t} + \mathbf{v_n} \cdot \nabla \phi = 0 & \text{in} \quad \Omega \\ \varepsilon_0 \nabla \cdot (-\varepsilon_r \nabla \varphi) = q \sum_{\alpha=1}^{M_{ion}} z_\alpha n_\alpha & \text{in} \quad \Omega_{dielectric} \\ \nabla \cdot (-\sigma \nabla \varphi) = \nabla \cdot (\sigma \nabla \alpha_T T) & \text{in} \quad \Omega_{metal}, \end{cases} \tag{17}$$

with

$$\mathbf{v_n} = v_n \mathbf{n} = \big(C_s \nabla \cdot (P_\phi \nabla K) + C_{el} \nabla \cdot (P_\phi \nabla E_n^2) + F(E_n) \big) \mathbf{n} \quad \text{in} \quad \Omega, \tag{18}$$

where we have exploited relation $\nabla_s \cdot = P_\phi \nabla \cdot$ between the surface gradient ∇_s and the standard operator ∇,

$$P_\phi = I - \frac{\nabla \phi}{||\nabla \phi||} \otimes \frac{\nabla \phi}{||\nabla \phi||} \tag{19}$$

denoting the projection matrix which extracts the normal direction to the surface S_g. Model (17) is completed with suitable boundary data, depending on the specific configuration. In particular, since both the curvature and the normal velocity vanish outside a narrow band close to S_g, we assign homogeneous Neumann boundary conditions on the whole boundary $\partial\Omega$ to the level-set function ϕ. Concerning function φ, we enforce non-homogeneous Dirichlet data on the electrical contacts, Γ_{top} and Γ_{bottom}, in order to enforce the bias voltage condition, while homogeneous Neumann boundary values are selected on Γ_N.

4.2 Dicretization of the PDE system

With the aim of providing a discrete counterpart to system (17), we need to consider several issues. First, we observe that system (17) is nonlinear since the level-set function in $(17)_1$ depends on the normal velocity $\mathbf{v_n}$ which, in turn, depends on ϕ through the curvature K (see relation (16)) and the projection matrix P_ϕ (see relation (19)). In addition, problems $(17)_1$ and $(17)_2$-$(17)_3$ are coupled due to the dependence of $\mathbf{v_n}$ on φ through the electric field, being $E_n = -\nabla \varphi \cdot \mathbf{n}$. As a second matter, we notice that only equation $(17)_1$ explicitly depends on the time. On the contrary, the temporal dependence of problem $(17)_2$-$(17)_3$ is implicit, being linked to the fact that domains $\Omega_{dielectric}$ and Ω_{metal} change as function of ϕ.

To approximate the temporal evolution, we introduce a uniform time partition characterized by the constant step Δt (we refer to the numerical validation for additional comments regarding the selection of this quantity).
In practice, at each time t of the temporal partition, under the assumption that $\phi = \phi^t$ is known: i) we update the dielectric and the metallic portions of Ω, i.e., we identify domains $\Omega^t_{dielectric}$ and Ω^t_{metal}; ii) we solve the generalized Poisson problem

$$\begin{cases} \varepsilon_0 \nabla \cdot (-\varepsilon_r \nabla \varphi^t) = q \sum_{\alpha=1}^{M_{ion}} z_\alpha n_\alpha & \text{in} \quad \Omega^t_{dielectric} \\ \nabla \cdot (-\sigma \nabla \varphi^t) = \nabla \cdot (\sigma \nabla \alpha_T T) & \text{in} \quad \Omega^t_{metal}, \end{cases} \tag{20}$$

to compute the normal electric field E^t_n associated with the potential φ^t; iii) we update the mean curvature K^t of the level-set function and the projection operator P^t_ϕ through relation (16) and (19), respectively; iv) we compute the surface velocity, $\mathbf{v}^t_\mathbf{n}$, as in (18); v) we evolve the level-set function from t to $t+\Delta t$, by solving problem $(17)_1$. In particular, the nonlinearity of this equation is addressed by explicitly treating the velocity, so that we have

$$\phi^{t+\Delta t} = \phi^t - \Delta t v^t_n \frac{\nabla \phi^t \cdot \nabla \phi^t}{||\nabla \phi^t||} = \phi^t - \Delta t v^t_n ||\nabla \phi^t||, \tag{21}$$

definition (15) being exploited. Of course, this time-stepping strategy has to be initialized through equations (13)-(14). We remark that items ii) and iv) enable the management of the coupling between problems $(17)_1$ and $(17)_2$-$(17)_3$. Moreover, analogous to what was observed in [7, 6], the straightforward computation of K^t and $\mathbf{v}^t_\mathbf{n}$ at items iii) and iv), followed by the evolution of ϕ^t in v) to time $t + \Delta t$ may result in numerical oscillations of the level-set function. To overcome this issue, we adopt a similar approach to that in [7]. Thus, the update of K^t in iii) through relation (16) is carried out by replacing ϕ^t with $\phi^{t+\Delta t}$, so that

$$K^t = \nabla \cdot \frac{\nabla(\phi^t - \Delta t v^t_n \|\nabla \phi^t\|)}{\|\nabla(\phi^t - \Delta t v^t_n \|\nabla \phi^t\|)\|}. \tag{22}$$

Hence, at each time t, assuming that $\phi = \phi^t$ is known, we need to solve the following mixed system in terms of curvature K^t and surface velocity v^t_n

$$\begin{cases} K^t + \nabla \cdot \left(\dfrac{\Delta t}{B} \|\nabla \phi^t\| \nabla v^t_n \right) = \nabla \cdot \left(\dfrac{1}{B} \nabla \phi^t \right) & \text{in} \quad \Omega \\ v^t_n - C_s \nabla \cdot \left(P_{\phi^t} \nabla K^t \right) = C_{el} \nabla \cdot \left(P_{\phi^t} \nabla (E^t_n)^2 \right) + F(E^t_n) & \text{in} \quad \Omega, \end{cases} \tag{23}$$

with $B = \| \nabla(\phi^t - \Delta t v^{t-\Delta t}_n \|\nabla \phi^t\|) \|$. With regard to (22), quantity B should be defined by $B = \| \nabla(\phi^t - \Delta t v^t_n \|\nabla \phi^t\|) \|$. The choice in (23) avoids addressing the nonlinearity, in accordance with [7]. Moreover, the differential problems in (23) are supplemented with fully homogeneous Neumann boundary conditions, analogous to the level-set function.
Solution to system (23) replaces the update of K^t and of $\mathbf{v}^t_\mathbf{n}$ at item iii) and iv) of the time-stepping procedure above. In particular, the second term on the left-hand side of the first equation, which couples K^t with v^t_n, acts as a regularization contribution of

the form Δv_n^t, with regularization parameter $\Delta t\|\nabla\phi^t\|/B$, thereby damping potential numerical instabilities.
Finally, by examining (18) and (16), it becomes evident that the surface velocity depends on the fourth-order spatial derivative of the level-set function. This issue will be addressed by adopting the weak form of system (23), in view of a finite element discretization of the spatial dependence.

4.2.1 Weak formulation

Equation (21) can be explicitly employed to track the time advancement of the conductor surface. On the contrary, the spatial dependence of the two problems in (23) as well as of the generalized Poisson equation in (20) still requires approximation. In the following, we focus on the discretization of (23), while referring to [27] for the numerical treatment of (20).
We introduce the space $V = H^1(\Omega)$. Then, the weak form of the two PDEs in (23) becomes: for each t, find $(K^t, v_n^t) \in V \times V$ such that, for any $(\overline{\psi}, \psi) \in V \times V$, it holds

$$\begin{cases} \displaystyle\int_\Omega K^t\overline{\psi}\,d\Omega - \frac{\Delta t}{B}\,\|\nabla\phi^t\| \int_\Omega \nabla v_n^t \cdot \nabla\overline{\psi}\,d\Omega = -\frac{1}{B}\int_\Omega \nabla\phi^t \cdot \nabla\overline{\psi}\,d\Omega \\ \displaystyle\int_\Omega v_n^t\,\psi\,d\Omega + C_s\int_\Omega P_{\phi^t}\nabla K^t \cdot \nabla\psi\,d\Omega = -C_{el}\int_\Omega P_{\phi^t}\nabla\big(E_n^t\big)^2 \cdot \nabla\psi\,d\Omega + \int_\Omega F(E_n^t)\psi\,d\Omega, \end{cases} \tag{24}$$

where we have exploited the boundary conditions assigned to K^t and v_n^t, along with the fact that both the level-set function and the normal electric field have a null gradient on the domain boundary.
With regard to the last term in the second equation, the particular choice made in (10) ensures it is well-defined.
In view of the Galerkin formulation, it is practical to rewrite (24) in the following way: for each t, find $\boldsymbol{u}^t = (K^t, v_n^t) \in V \times V$ such that, for any $(\overline{\psi}, \psi) \in V \times V$, we have

$$\begin{cases} a_K(\boldsymbol{u}^t, \overline{\psi}) = f_K(\overline{\psi}) \\ a_{v_n}(\boldsymbol{u}^t, \psi) = f_{v_n}(\psi), \end{cases} \tag{25}$$

with

$$\begin{aligned} a_K(\boldsymbol{u}^t, \overline{\psi}) &= \textstyle\int_\Omega K^t\overline{\psi}\,d\Omega - \dfrac{\Delta t}{B}\,\|\nabla\phi^t\| \displaystyle\int_\Omega \nabla v_n^t \cdot \nabla\overline{\psi}\,d\Omega, \\ a_{v_n}(\boldsymbol{u}^t, \psi) &= \displaystyle\int_\Omega v_n^t\,\psi\,d\Omega + C_s\int_\Omega P_{\phi^t}\nabla K^t \cdot \nabla\psi\,d\Omega \end{aligned}$$

the bilinear forms associated with equation $(24)_1$ and $(24)_2$, respectively,

$$\begin{aligned} f_K(\overline{\psi}) &= -\frac{1}{B}\int_\Omega \nabla\phi^t \cdot \nabla\overline{\psi}\,d\Omega \\ f_{v_n}(\psi) &= -C_{el}\textstyle\int_\Omega P_{\phi^t}\nabla(E_n^t)^2 \cdot \nabla\psi\,d\Omega + \displaystyle\int_\Omega F(E_n^t)\psi\,d\Omega. \end{aligned}$$

the corresponding linear forms.

4.2.2 The Galerkin finite element approximation

The discrete counterpart of equations (25) is obtained by employing a Galerkin formulation. To this aim, we introduce a conformal triangular tessellation, $\mathcal{T}_h = \{K\}$, of the computational domain Ω, along with an associated finite-dimensional space $V_h \subset V$, with $N_h = \dim(V_h)$ [19].
The selection of the computational mesh in modeling the CF evolution is a crucial step. Indeed, since the dielectric and metal subdomains evolve over time, a fixed grid might not be suited to discretize any configuration Ω_{metal} and $\Omega_{dielectric}$ assume. Furthermore, the width of the CF is generally much smaller than the dimension of Ω. Therefore, employing a uniform mesh with a discretization step small enough to accurately capture the CF evolution might result in an unfeasible computational burden. These challenges justify the utilization of an adaptive computational mesh, which evolves over time, as explained in the following section.

The Galerkin approximation to (25) is obtained as follows: for each t, find $\boldsymbol{u}_h^t = (K_h^t, v_{n,h}^t) \in V_h \times V_h$ such that, for any $(\overline{\psi}_h, \psi_h) \in V_h \times V_h$, we solve

$$\begin{cases} a_K(\boldsymbol{u}_h^t, \overline{\psi}_h) = f_K(\overline{\psi}_h) \\ a_{v_n}(\boldsymbol{u}_h^t, \psi_h) = f_{v_n}(\psi_h). \end{cases} \tag{26}$$

In particular, the numerical validation in Sec. 5 is performed by employing a Galerkin finite element discretiazion, which is equivalent to choosing

$$V_h = X_h^1(\Omega) \equiv \{w_h \in \mathcal{C}^0(\overline{\Omega}) : w_h|_K \in \mathbb{P}_1(K) \ \forall K \in \mathcal{T}_h\}, \tag{27}$$

namely, the space of piecewise linear polynomials associated with the partition $\mathcal{T}_h$ of Ω [19].
To switch to the algebraic form of system (26), we introduce a Lagrangian basis, $\{\psi_j\}_{j=1}^{N_h}$, for the space V_h. Consequently, the discrete curvature and normal velocity can be expressed as linear combinations of this basis, as $K_h^t = \sum_{j=1}^{N_h} k_j^t \psi_j$ and $v_{n,h}^t = \sum_{j=1}^{N_h} v_{n,j}^t \psi_j$. Using these expansions in (26) and choosing $\overline{\psi}_h = \psi_h = \psi_i$, we are thus led to solve the system

$$\begin{bmatrix} A & C \\ C & \tilde{A} \end{bmatrix} \begin{bmatrix} \mathbf{v}_{n,h}^t \\ \mathbf{K}_h^t \end{bmatrix} = \begin{bmatrix} \mathbf{F}_{v_n} \\ \mathbf{F}_k \end{bmatrix}, \tag{28}$$

where vectors $\mathbf{v}_{n,h}^t$ and $\mathbf{K}_h^t$ gather the unknown coefficients $\{v_{n,j}^t\}_{j=1}^{N_h}$ and $\{k_j^t\}_{j=1}^{N_h}$, respectively, while the components of the block matrix and of the right-hand side are defined by

$$A_{ij} = -\frac{\Delta t}{B_h} \|\nabla \phi_h^t\| \int_\Omega \nabla\psi_j \cdot \nabla\psi_i \, d\Omega, \quad \tilde{A}_{ij} = C_s \int_\Omega P_{\phi_h^t} \nabla\psi_j \cdot \nabla\psi_i \, d\Omega, \quad C_{ij} = \int_\Omega \psi_j \psi_i \, d\Omega, \tag{29a}$$

$$F_{v_n,i} = -\frac{1}{B_h} \int_\Omega \nabla\phi_h^t \cdot \nabla\psi_i \, d\Omega, \quad F_{k,i} = -C_{el} \int_\Omega P_{\phi_h^t} \nabla (E_{n,h}^t)^2 \cdot \nabla\psi_i \, d\Omega + \int_\Omega F(E_{n,h}^t)\psi_i \, d\Omega, \tag{29b}$$

for $i,\ j = 1, \ldots, N_h$. Here, ϕ_h^t denotes the projection of the level-set function onto V_h at time t, the norm B_h and the projection matrix $P_{\phi_h^t}$ being defined accordingly; $E_{n,h}^t = -\nabla\varphi_h^t \cdot \mathbf{n}$ represents the approximation of the electric field normal to the surface S_g computed through the discrete solution φ_h^t to the generalized Poisson equation (20) (see [27]).

5 Mesh adaptation algorithms

The use of a computational mesh tailored to the specific problem is widely acknowledged to either significantly reduce the computational cost while maintaining a certain level of accuracy in the computed solution or, alternatively, substantially increase the solution accuracy without exceeding a fixed computational cost [42, 48]. The use of an adaptive mesh procedure is particularly effective when dealing with moving boundaries. This is exactly the case of the CF modeling described in Sec. 2

In this study, we utilize both isotropic grids (equilateral triangles with varying sizes) and anisotropic grids (triangles characterized by varying shapes, sizes, and orientations) in the mesh adaptation process. In both cases, the mesh adaptation is guided by a recovery-based error estimator, as described in [63, 64] and [36], respectively. The selection of this particular error estimator is driven by its proven effectiveness and ease of implementation, as demonstrated in the existing literature [60, 20, 43, 38, 34].

5.1 The adaptation scheme

We employ a mesh adaptation procedure that has been successfully validated in various application scenarios, both in isotropic and anisotropic contexts. The idea we implement is to construct an optimized (adapted) mesh that allows us to ensure a desired accuracy on the approximation provided by the chosen discretization scheme, when used as a surrogate for the exact solution. Simultaneously, we aim to minimize the number of the grid triangles and to equidistribute the error throughout the mesh elements.
The mesh optimization is carried out through the concept of metric, i.e., of mesh spacing [22]. Starting from the approximate solution, the associated discretization error is estimated, allowing the prediction of the new element distribution. In particular, more triangles will be allocated in the areas where the estimator of the error is higher and vice versa. To this end, we employ an iterative procedure that, starting from an initial uniform grid, $\mathcal{T}_h^{(0)}$, constructs the adapted grid. In particular, at the generic i-th iteration, we carry out the following operations:

i) we compute the discrete solution associated with the current mesh, $\mathcal{T}_h^{(i)}$;

ii) we evaluate the corresponding error estimator, $\mathcal{S}^{(i)}$;

iii) from the estimator, we derive the new metric, $\mathcal{M}^{(i+1)}$ which guarantees the desired accuracy, `TOL`, the minimization of the mesh elements and the error equidistribution;

iv) we employ the metric $\mathcal{M}^{(i+1)}$ to generate the new adapted mesh $\mathcal{T}_h^{(i+1)}$.

The adaptive loop is terminated when the number of elements that change between two successive iterations falls below a user-defined percentage.
In the following we discuss in details steps ii) and iii), which constitute the most technical part of the adaptive procedure. Step iv) turns out to be straightforward when dealing with a mesh generator that supports the concept of a metric.

5.1.1 The isotropic error estimator

We employ a recovery-based error estimator among the several options available in the literature [1]. This choice is motivated by the many positive properties characterizing such estimators, primarily the exceptional performance despite an extremely simple implementation. To this aim, we first select a reference physical quantity, q, to optimize the mesh with respect to. Then, following the original idea proposed by O.C. Zienkiewicz, J.Z. Zhu [64, 63], we construct an estimate for the $H^1(\Omega)$-seminorm of the discretization error,

$$|q - q_h|^2_{H^1(\Omega)} = \|\nabla q - \nabla q_h\|^2_{L^2(\Omega)}, \tag{30}$$

simply replacing the (generally unknown) gradient of the exact solution with the so-called recovered gradient, $\nabla^* q_h$, so that the reference error estimator, η, reads as

$$\eta^2 = \|\nabla^* q_h - \nabla q_h\|^2_{L^2(\Omega)}. \tag{31}$$

Unlike the exact gradient, quantity $\nabla^* q_h$ is computable, generally coinciding with a suitable average or projection of the discrete gradient, ∇q_h, onto a subset of grid elements. This feature makes η an a posteriori error estimator. Moreover, we observe that, for mesh adaptation purposes, it is useful to rewrite the estimator η by separating the information associated with individual triangles, namely as

$$\eta^2 = \sum_{K \in \mathcal{T}_h} \eta_K^2 \quad \text{with} \quad \eta_K^2 = \|\nabla^* q_h - \nabla q_h\|^2_{L^2(K)}. \tag{32}$$

For modeling the evolution of the CF, we adopt the level-set function as the quantity driving the mesh adaptation, thus setting $q = \phi^t$, $q_h = \phi_h^t$ in (30)-(32). This choice will enable an accurate tracking of any change in the topology of the curve S_g, thus precisely locating, at each time, the portions of metal and dielectric where the generalized Poisson equation needs to be solved. In particular, we use a smoothed variant, $\phi^{t,s}$, of the level-set function in order to minimize possible numerical instabilities [14]. Among the possible choices in the literature, we select $\phi^{t,s}$ as the solution to the Helmholtz equation

$$\begin{cases} -\lambda^2 \nabla^2 \phi^{t,s} + \phi^{t,s} = \phi^t & \text{in} \quad \Omega \\ \lambda^2 \nabla \phi^{t,s} \cdot \mathbf{n} = 0 & \text{on} \quad \partial\Omega, \end{cases} \tag{33}$$

where λ is an empirical parameter tuning the thickness of the smoothing.

Concerning the recovered gradient, we identify $\nabla^*\phi_h^{t,s}$ with the area-weighted average of the discrete gradient over a suitable patch of elements of the mesh [36]. In particular, $\nabla^*\phi_h^{t,s}$ coincides with a function which is piecewise constant on $\mathcal{T}_h$, such that the recovered value on the element $K \in \mathcal{T}_h$ is given by

$$\nabla^*\phi_h^{t,s}(\mathbf{x}) = \frac{1}{|\Delta_K|} \sum_{T \in \Delta_K} |T| \, \nabla\phi_h^{t,s}\big|_T \tag{34}$$

with $\mathbf{x} \in K$, Δ_K the patch of elements associated with K and where $|\omega|$ denotes the measure of the generic subset $\omega \subset \mathbb{R}^2$. Notation

$$\eta^2_{\phi^{t,s}} = \sum_{K \in \mathcal{T}_h} \eta^2_{K,\phi^{t,s}} \quad \text{with} \quad \eta^2_{K,\phi^{t,s}} = \|\nabla^*\phi_h^{t,s} - \nabla\phi_h^{t,s}\|^2_{L^2(K)}, \tag{35}$$

$\nabla^*\phi_h^{t,s}$ defined as in (34), will be adopted throughout the paper to refer to the recovery-based error estimator used to control the seminorm $|\phi^{t,s} - \phi_h^{t,s}|_{H^1(\Omega)}$.

5.1.2 The anisotropic error estimator

The anisotropic counterpart of estimator $\eta^2_{\phi^{t,s}}$ is formalized in the anisotropic setting proposed in [21]. Here, the authors characterize the size, the shape and the orientation of each mesh element $K \in \mathcal{T}_h$ through the spectral properties of the affine map $T_K : \hat{K} \to K$ which changes the reference triangle $\hat{K}$ and the circumscribed circle into the generic element K and the circumscribed ellipse (see Fig. 4). In particular, the directions, $\mathbf{r}_{i,K}$, and the lengths, $\lambda_{i,K}$, of the semi-axes of this ellipse identify the geometric features of K, constituting the so-called elemental metric $\mathcal{M}_K = \{\mathbf{r}_{i,K}, \lambda_{i,K}\}_{i=1}^2$.
When K is given, it is customary to retrieve the metric information by first calculating the polar decomposition, $M_K = B_K Z_K$, of the Jacobian matrix, $M_K \in \mathbb{R}^{2\times 2}$, of the map T_K, where $B_K \in \mathbb{R}^{2\times 2}$ is symmetric positive definite and $Z_K \in \mathbb{R}^{2\times 2}$ is orthogonal. Subsequently, the spectral decomposition $B_K = R_K^T \Lambda R_K$ of the matrix B_K is performed, where $R_K^T = [\mathbf{r}_{1,K}, \mathbf{r}_{2,K}]$ and $\Lambda_K = \mathrm{diag}(\lambda_{1,K}, \lambda_{2,K})$ denote the eigenvector and eigenvalue matrix, respectively.

According to [36], the anisotropic error estimator for the seminorm $|\phi^{t,s} - \phi_h^{t,s}|_{H^1(\Omega)}$, which generalizes $\eta^2_{\phi^{t,s}}$, is given by

$$\Xi^2_{\phi^{t,s}} = \sum_{K \in \mathcal{T}_h} \Xi^2_{K,\phi^{t,s}} \quad \text{with} \quad \Xi^2_{K,\phi^{t,s}} = \frac{1}{\lambda_{1,K}\lambda_{2,K}} \sum_{i=1}^{2} \lambda_{i,K}^2 \Big[\mathbf{r}_{i,K}^T G_{\Delta_K}(\nabla^*\phi_h^{t,s} - \nabla\phi_h^{t,s})\mathbf{r}_{i,K}\Big], \tag{36}$$

where $G_{\Delta_K}(\cdot) \in \mathbb{R}^{2\times 2}$ is the symmetric semi-definite positive matrix with entries

$$[G_{\Delta_K}(\mathbf{w})]_{i,j} = \sum_{T \in \Delta_K} \int_T w_i w_j \, dT, \tag{37}$$

with i, $j = 1$, 2, and for any vector-valued function $\mathbf{w} = [w_1, w_2]^T \in \big[L^2(\Omega)\big]^2$. Matrix G_{Δ_K} separates the components of the isotropic error estimator in (35) and project them

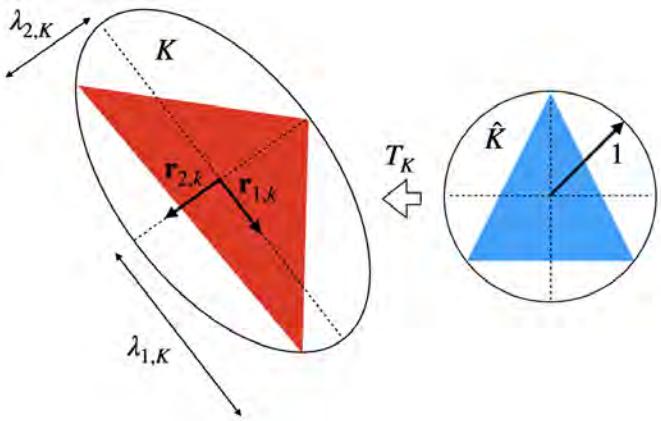

Figure 4: Sketch of the affine map T_K.

along the anisotropic directions. This is a classical approach according to the theory in [21] to recover anisotropic information starting from an isotropic quantity. Finally, the scaling factor $\left[\lambda_{1,K}\lambda_{2,K}\right]^{-1}$ guarantees the consistency of the anisotropic estimator with the isotropic one.

5.1.3 The metric

In the following, we focus on the anisotropic context, as the isotropic case represents a subset of it (see Remark 5.1). The derivation of a metric $\mathcal{M}$ from the error estimator in (36) is constrained by three specific criteria that the new adapted mesh has to take into account: an accuracy requirement on the estimator $\Xi^2_{\phi^{t,s}}$, the minimization of the mesh cardinality and the equidistribution of the error across the adapted grid.
Such requirements translate into solving a constrained optimization problem. In particular, to minimize the mesh cardinality, $\#\mathcal{T}_h$, we rescale the local estimator $\Xi^2_{K,\phi^{t,s}}$ with respect to the area of the patch, so that

$$\begin{aligned}\Xi^2_{K,\phi^{t,s}} &= |\hat{\Delta}_K|\lambda_{1,K}\lambda_{2,K}\Bigg[s_K\Big(\mathbf{r}^T_{1,K}\,\tilde{G}_{\Delta_K}(\nabla^*\phi_h^{t,s}-\nabla\phi_h^{t,s})\mathbf{r}_{1,K}\Big)\\ &+ \frac{1}{s_K}\Big(\mathbf{r}^T_{2,K}\,\tilde{G}_{\Delta_K}(\nabla^*\phi_h^{t,s}-\nabla\phi_h^{t,s})\mathbf{r}_{2,K}\Big)\Bigg],\end{aligned}$$

where $\hat{\Delta}_K = T_K^{-1}(\Delta_K)$ is the pullback patch via map T_K, $s_K = \lambda_{1,K}/\lambda_{2,K} \geq 1$ denotes the aspect ratio of the element K, measuring the deformation of the triangle, $\tilde{G}_{\Delta_K}(\cdot) = G_{\Delta_K}(\cdot)/|\Delta_K|$ is the scaled counterpart of the matrix defined in (37). The connection between minimizing the mesh cardinality and maximizing the element area, along with the equidistribution of the error (i.e., $\Xi^2_{K,\phi^{t,s}} = \texttt{TOL}^2/\#\mathcal{T}_h$, where $\texttt{TOL}$ represents the accuracy specified by the user for the global estimator, results in addressing the following

constrained minimization problem for each element K of $\mathcal{T}_h$:

$$\min_{s_K,\mathbf{r}_{i,K}} \mathcal{S}_K\Big(s_K,\{\mathbf{r}_{i,K}\}_{i=1}^2\Big) \quad \text{s.t.} \quad \begin{cases} \mathbf{r}_{i,K}\cdot\mathbf{r}_{j,K}=\delta_{ij} \\ s_K \geq 1, \end{cases} \tag{38}$$

with δ_{ij} the Kronecker symbol, and where

$$\begin{aligned} \mathcal{S}_K\Big(s_K,\{\mathbf{r}_{i,K}\}_{i=1}^2\Big) &= s_K\Big(\mathbf{r}_{1,K}^T\,\tilde{G}_{\Delta_K}(\nabla^*\phi_h^{t,s}-\nabla\phi_h^{t,s})\mathbf{r}_{1,K}\Big) \\ &+ \frac{1}{s_K}\Big(\mathbf{r}_{2,K}^T\,\tilde{G}_{\Delta_K}(\nabla^*\phi_h^{t,s}-\nabla\phi_h^{t,s})\mathbf{r}_{2,K}\Big). \end{aligned}$$

It can be proved that problem (38) admits the explicit solution

$$s_K^{\mathcal{O}p}=\sqrt{\frac{g_{1,K}}{g_{2,K}}}, \qquad \mathbf{r}_{1,K}^{\mathcal{O}p}=\mathbf{g}_{2,K}, \qquad \mathbf{r}_{2,K}^{\mathcal{O}p}=\mathbf{g}_{1,K},$$

with $\{g_{i,K},\mathbf{g}_{i,K}\}_{i=1}^2$ the eigenpairs associated with matrix $\tilde{G}_{\Delta_K}(\nabla^*\phi_h^{t,s}-\nabla\phi_h^{t,s})$ [35, 34]. The error equidistribution is finally exploited to derive the two optimal anisotropic lengths, $\lambda_{1,K}^{\mathcal{O}p}$ and $\lambda_{2,K}^{\mathcal{O}p}$, from the aspect ratio $s_K^{\mathcal{O}p}$, thus obtaining

$$\lambda_{1,K}^{\mathcal{O}p}=g_2^{-1/2}\left(\frac{\texttt{TOL}^2}{2\,\#\mathcal{T}_h\,|\hat{\Delta}_K|}\right)^{1/2}, \quad \lambda_{2,K}^{\mathcal{O}p}=g_1^{-1/2}\left(\frac{\texttt{TOL}^2}{2\,\#\mathcal{T}_h\,|\hat{\Delta}_K|}\right)^{1/2}. \tag{39}$$

The optimal quantities $\lambda_{i,K}^{\mathcal{O}p}$ and $\mathbf{r}_{i,K}^{\mathcal{O}p}$, $i=1,2$, form the optimal metric $\mathcal{M}_K$ predicted by the error estimator for the element K. Hence, the overall metric $\mathcal{M}=\{\mathcal{M}_K\}$ contains the information to be utilized as input for a metric-based mesh generator to construct the new adapted mesh.

Remark 5.1 (The isotropic metric) *According to [34], it can be proved that the isotropic counterpart of the optimal metric $\mathcal{M}_K$ is obtained by solving problem* (38) *with the constraint $s_K=1$. This leads to the optimal lengths*

$$\lambda_{1,K}^{\mathcal{O}p}=\lambda_{2,K}^{\mathcal{O}p}=\Big(\frac{g_1+g_2}{2}\Big)^{-1/2}\left(\frac{\texttt{TOL}^2}{2\,\#\mathcal{T}_h\,|\hat{\Delta}_K|}\right)^{1/2}.$$

6 The numerical scheme

We now have all the tools needed to assemble the whole computational procedure for modeling the evolution of the CF. Figure 5 shows how we combine these tools, distinguishing between the case where computational mesh adaptation is activated and when it is not.

We start by considering the tessellation $\mathcal{T}_h=\mathcal{T}_h^{(0)}$ of the domain Ω and we inizialize the discrete level-set function, ϕ_h^0, by projecting function ϕ_0 in (13)-(14) onto V_h. Subsequently, the workflow either engages in mesh adaptation or proceeds without it. In both scenarios, while assuming the knowledge of the level-set function ϕ_h^t at time t, the subsequent operations are iteratively performed:

1) we discretize the generalized Poisson equation (20) on the domains $\Omega^t_{dielectric}$, Ω^t_{metal} to compute the normal electric field $E^t_{n,h}$;

2) we update the mean curvature K^t_h and the normal velocity $v^t_{n,h}$ of the surface through relation (16) and (18), respectively;

3) we evolve the level-set discrete function from t to $t + \Delta t$ through relation (21).

The enhancement of this procedure with mesh adaptation implies, before executing steps 1)-3), an update of the mesh driven by the metric $\{\lambda^{\mathcal{O}p}_{i,K}, \mathbf{r}^{\mathcal{O}p}_{i,K}\}$ followed by a projection of the level-set function, along with all the physical quantities defined on the current mesh, onto the adapted mesh. Notice that at the initial time the mesh adaptation is carried out starting from a uniform mesh of Ω.

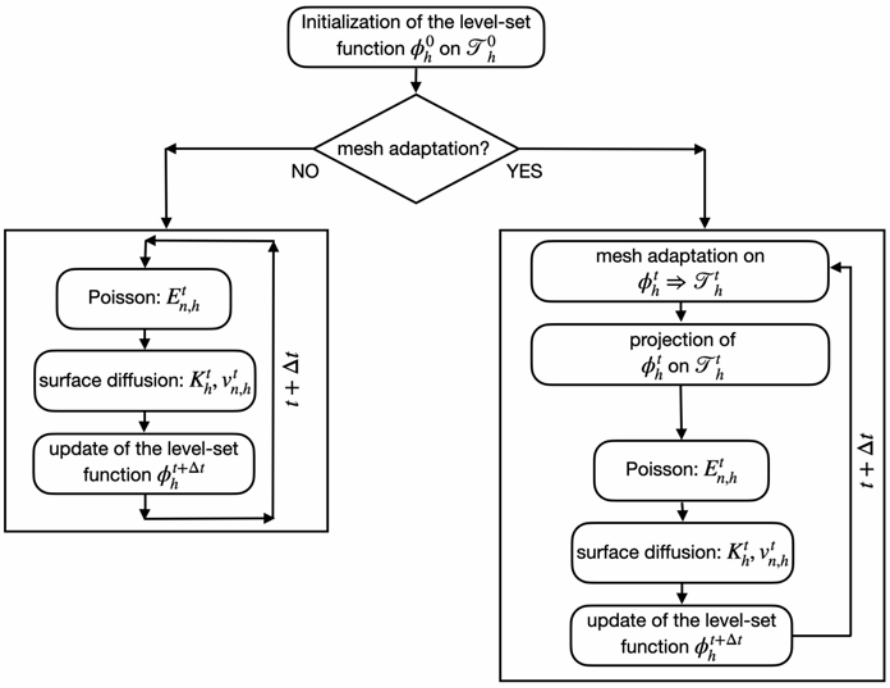

Figure 5: Flow chart of the computational scheme.

7 Numerical results

The workflow in Fig. 5 has been implemented on the FEMOS-MP (Finite Element Modeling-Oriented Simulator for Multi-Physics simulation) platform [29, 45, 27].
FEMOS-MP is a C++ modular code operating in both $2D$ and $3D$ frameworks. In particular, we have incorporated the Mmg library ([17]) for mesh adaptation purposes.

7.1 Test 1: Surface diffusion due to curvature gradient

This section presents the evolution of two different shapes under the influence of the surface diffusion, without including the effect of the electric field ($E_n^t = 0$ in (23), for any t) and without resorting to mesh adaptation. In both cases we choose the square computational domain $\Omega = (0,1)^2$ that we discretize with a triangular structured mesh consisting of 66048 elements, with a maximum element diameter $h = 0.006$.

The first shape is an ellipse with horizontal and vertical semi-axes of length 0.3 and 0.2, respectively. Moreover, we set $C_s = 10^{-3}$ in (23). The evolution of the shape is shown in Fig. 6, for a time step $\Delta t = 10^{-3}s$. As expected, the ellipse evolves into a circle, which represents the stable configuration for the surface diffusion, minimizing the surface energy [10, 4].

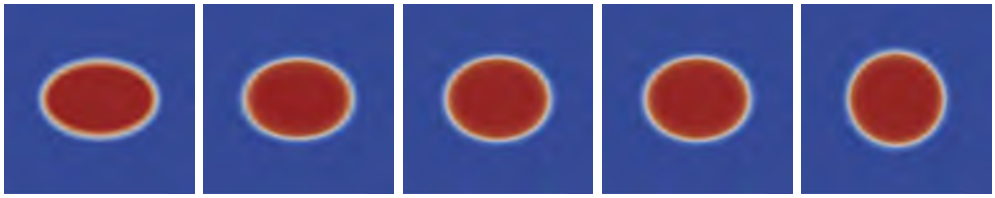

Figure 6: Evolution of an ellipse into a circle under the effect of the surface diffusion due to curvature gradient: $t = 0s, 0.1s, 0.2s, 0.3s, 1s$ (from left to right).

The second shape is a star consisting of two ellipses with semi-axes of lengths 0.4 and 0.075, rotated relative to each other by an angle of 45^o. The time evolution under the Laplacian of the curvature is displayed in Fig. 7, for $C_s = 10^{-4}$ and $\Delta t = 10^{-3}s$. Also in this case, the surface changes from the initial shape to the stable circular configuration.

Figure 7: Evolution of a star into a circle under the effect of the surface diffusion due to curvature gradient: $t = 0s, 0.1s, 0.3s, 0.4s, 1s$ (from left to right).

7.2 Test 2: Effects of an applied electric field

The inclusion of the electric field effect in (23) considerably increases the model complexity, often resulting in a prohibitive computational cost, even for simple geometries. For this reason, the use of mesh adaptation becomes necessary. Both isotropic and anisotropic mesh adaptation strategies are employed in the following.

In a first case, we explore the effect of the electric field on the transformation of a stable shape (circle) into an unstable shape (ellipse), where stability and instability are defined with respect to the effect of the curvature gradient. In other words, the dynamics are now governed by the electro-mechanical stress rather than by the curvature gradient. The electric field strength is generated by applying a voltage difference of $1V$ between the Γ_{top} (positively biased) and Γ_{bottom} (grounded) edges. The initial shape is a circle with a radius approximately equal to 0.245 composed of a metallic material, while the remaining simulation domain consists of a dielectric, with $\varepsilon_r = 10$. Referring to (9)-(10), we set $C_s = 10^{-3}$, $C_{el} = 12 \cdot 10^{-4}$, $F(E_n) = 0$ and we choose $\Delta t = 10^{-3}$ as time step to discretize the time window.
Fig. 8 illustrates the transformation of the circle into an ellipse, with a major semi-axes aligned with the direction of the electric field. This behavior is consistent with the theoretical predictions [37] and has also been observed in the case of conductive liquid drops immersed in an electric field [53, 25]. In the panels of the first row, we present the simulation results for the isotropic mesh adaptation case, while in the second row, we show the anisotropic case. Both approaches exhibit similar behavior, although anisotropic mesh adaptation demonstrates superior computational time efficiency (32 minutes compared to 45 minutes). This improvement is attributed to the reduced number of elements, with 3586 in the anisotropic case versus 5532 in the isotropic case.
Fig. 9 illustrates the dynamic evolution of the electric field under anisotropic mesh

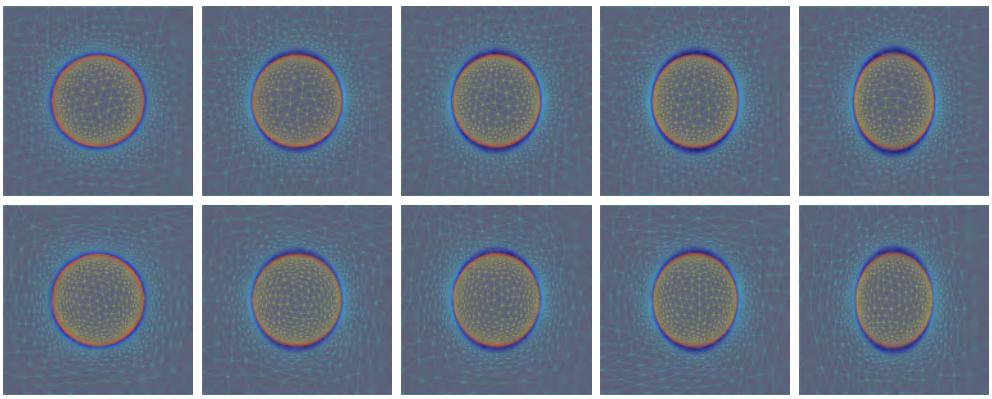

Figure 8: Evolution of a circle into an ellipse under the effect of the electromechanical stress, with $F(E_n) = 0$: isotropic (top) and anisotropic (bottom) adapted meshes, at $t = 0s, 0.1s, 0.2s, 0.3s, 0.8s$ (from left to right).

adaptation. As expected from physical considerations - specifically, the alignment between the ellipse major axis and the electric field direction - the electric field strength increases in the region enclosed between the evolving ellipse (resulting from the circle evolution) and the Γ_{top} and Γ_{bottom}.

In a second case, we investigate the effect of the electric field on the shape evolution of a circular metallic drop. The electric field strength is achieved by applying a voltage of $1V$ between Γ_{top} (positively biased) and Γ_{bottom} (grounded). The metallic drop has

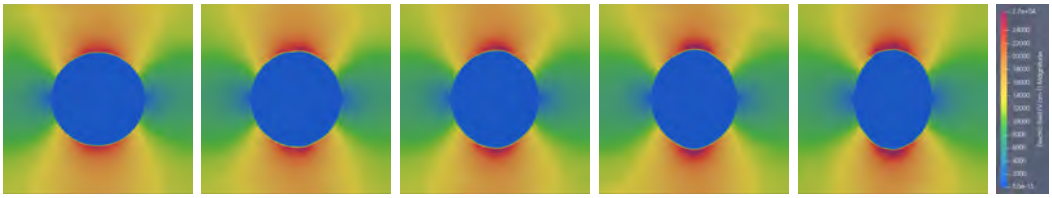

Figure 9: Evolution of a circle into an ellipse under the effect of the electromechanical stress, with $F(E_n) = 0$: electric field distribution with anisotropic mesh adaptation, at $t = 0s, 0.1s, 0.2s, 0.3s, 0.8s$ (from left to right).

an initial radius r equal to 0.245, while the dielectric part is characterized by $\varepsilon_r = 10$. With relation to (9), we set $C_s = 10^{-3}$, $C_{el} = 0$, while we choose $F(E_n) = C_{er}\, E_n$ with $C_{er} = 8 \cdot 10^{-2}$, and a time step $\Delta t = 10^{-3}$.
In this configuration, the electromechanical stress is inhibited in order to highlight the effect of the term $F(E_n)$ on the shape evolution. The primary consequence of mass injection from Γ_{top} towards the upper part of the circle, coupled with mass ejection from the bottom part toward Γ_{bottom}, results in an noticeable shift of the circle toward the top contact (see Fig. 10). As expected, with the movement of the metallic circle towards Γ_{top}, the strength of the electric field increases in the region delimited by the circle and Γ_{top}, while it decreases in the region between the circle and Γ_{bottom} (see Fig. 11). Moreover, the shape modulation induced by the effect of the surface diffusion occurs at a much slower rate compared to the drift. Therefore, it constitutes a negligible factor in the evolution of the circle's shape.

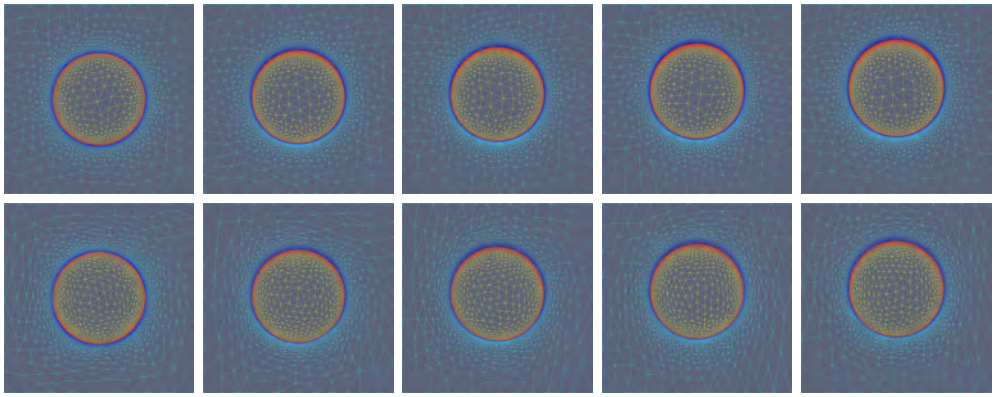

Figure 10: Evolution of a circular metallic drop under the effect of $F(E_n) = C_{er}\, E_n$: isotropic (top) and anisotropic (bottom) adapted meshes, at $t = 0s, 0.2s, 0.4s, 0.6s, 0.8s$ (from left to right).

Finally, Fig. 10 confirms the advantages brought about by anisotropic meshes, illustrating the evolution of the drop when using both an isotropic (first row) and an anisotropic (second row) adapted mesh. As in the earlier scenario, both approaches demonstrate comparable behavior. However, the use of anisotropic adaptation showcases superior

computational efficiency, completing the task in 23 minutes as opposed to 37 minutes, attributed to the decreased number of elements (3665 versus 7031).

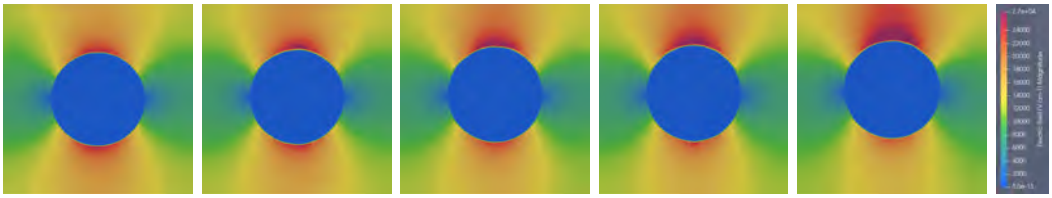

Figure 11: Evolution of a circular metallic drop under the effect of $F(E_n) = C_{er}\, E_n$: electric field distribution with anisotropic mesh adaptation, at $t = 0s, 0.2s, 0.4s, 0.6s, 0.8s$ (from left to right).

8 Simulation of the filament growth and dissolution in cation-based RRAM devices

This section focuses on the simulation of CF growth and dissolution in cation-based RRAM devices. The primary goal is to illustrate that the model and numerical methods outlined in Sec. 2 and Sec. 4 are capable of addressing both aspects within a physics-based context.

We begin by detailing the CF morphological changes, followed by an analysis of the corresponding variation in device resistance. To simulate these scenarios realistically, we scaled the computational domain to dimensions representative of actual cells, specifically setting to 10 nm the distance between the top and bottom contacts, and to 60 nm the domain width. Concerning the boundary conditions for the generalized Poisson equation (8), we assign $\varphi = 0.9V$ on Γ_{top} and $\varphi = 0V$ on Γ_{bottom} for the growth step. In the dissolution phase, we assign homogeneous data to both contacts, with the appropriate work function.

Table 1 provides the model coefficients and the numerical parameters utilized in the simulations for both CF growth and dissolution. We choose a value for C_s within the range employed in [56, 55] for similar materials, and we opt for a C_r value that lies moderately between those reported in [32, 11]. Material-dependent parameter values are selected to align with literature values for the RRAM structure $Ag/SiO_x/Pt$.

Finally, in all these simulations, we employ the anisotropic mesh adaptation strategy outlined in Sec. 5.

Table 1: Table of model coefficients and numerical parameters.

C_s	$10^{-31}\,[m^4/s]$	C_r	$3 \cdot 10^{-7}\,[m/s]$	C_{el}	$0\,[F \cdot m^3]$
T	$300\,[K]$	Δt	$0.1\,[\mu s]$ (growth), $10\,[\mu s]$ (dissolution)	ε	$6\varepsilon_0$
γ	$4.16 \cdot 10^{-23}\,[C\mu m]$	k	$1.38 \cdot 10^{-23}\,[J/K]$	ε_0	$8.854 \cdot 10^{-12}\,[F/m]$

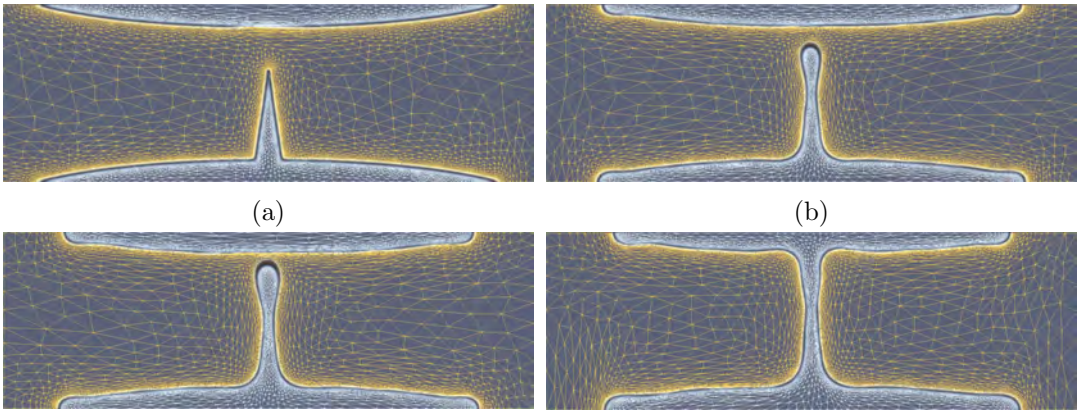

Figure 12: CF growth in a cation-based RRAM device: evolution of the anisotropic adapted mesh at $t = 0\,\mu s, 10\,\mu s$ (top) $t = 20\,\mu s, 40\,\mu s$ (bottom).

8.1 The filament growth

We refer to Sec. 2.2 for details on the constitutive laws used in simulating the CF growth. Fig. 12 shows the CF growth, starting from an initial triangular shape connected to the bottom electrode (panel (a)). The growth initiates from the bottom (inert) electrode, Γ_{bottom}, following an oxidation/reduction-limited regime as discussed in [61]. The CF gradually extends towards the top electrode, as shown in panels (b) and (c), ultimately producing a galvanic contact and creating a short circuit between the top and bottom electrodes (panel (d)). Specifically, in Fig. 12, the mesh evolution during the forming process is depicted: the white-meshed region corresponds to positive values of the level-set function, while the yellow-colored triangles represent the mesh elements with $\phi_h^t < 0$. In a parallel manner, the white-meshed region physically represents the evolution of metallic regions, whereas the yellow-meshed region represents the dielectric material. It is important to note that the metal contacts, whether made of Ag or Pt, are also represented in the white mesh.

Through our modeling, we can not only observe the shape evolution of the CF (Fig.12) but also analyze key physical quantities during CF growth, including the electrostatic potential (Fig.13, left column) and the electric field (Fig.13, right column). During the entire CF growth process, the voltage applied between the two electrodes remains constant. Consequently, far from the region of CF protrusion, the electrostatic potential across the dielectric is linear and remains constant over time, as illustrated in Fig.13 (left column). However, in the region where the CF connects to the top electrode, the electric potential undergoes significant modifications throughout the entire growth process (Fig.13, left column). This phenomenon is further highlighted by observing the electric field (Fig. 13, right column), which intensifies as the gap between the CF and the top electrode diminishes. Notably, the high electric field region extends beyond the lateral dimension of the CF, contributing to the rounded shape at the top of the CF.

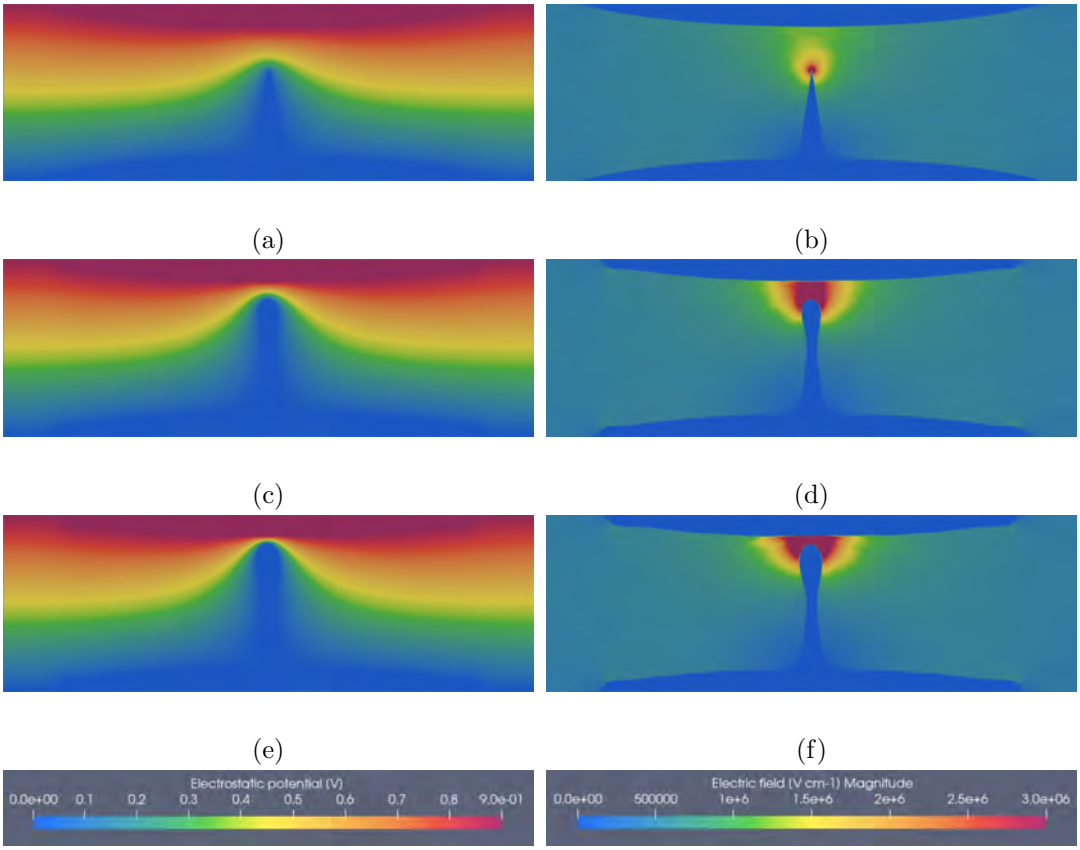

Figure 13: CF growth in a cation-based RRAM device: evolution of the electric potential (left) and of the electric field (right) at $t = 0\,\mu s$ (top), $t = 10\,\mu s$ (middle), $t = 20\,\mu s$ (bottom).

Additionally, consistent with physical expectations, the electric field diminishes to zero within the CF.

8.2 The filament dissolution

As mentioned in Sec.1, our modeling approach can also simulate filament dissolution. This has been explored by other authors, such as in [56], where the emphasis is primarily on the surface of the CF, neglecting the internal part, in contrast to our approach.
We emphasize that filament dissolution is entirely governed by the surface diffusion process, as no voltage is applied to the top or bottom electrode. This condition is achieved by setting $E_n = 0$ in (9), consistently with the approach in [56]. As an initial condition, we consider two superimposed triangles (one facing up and one facing down) penetrating to a specified depth, thereby controlling the CF dimension d. The impact

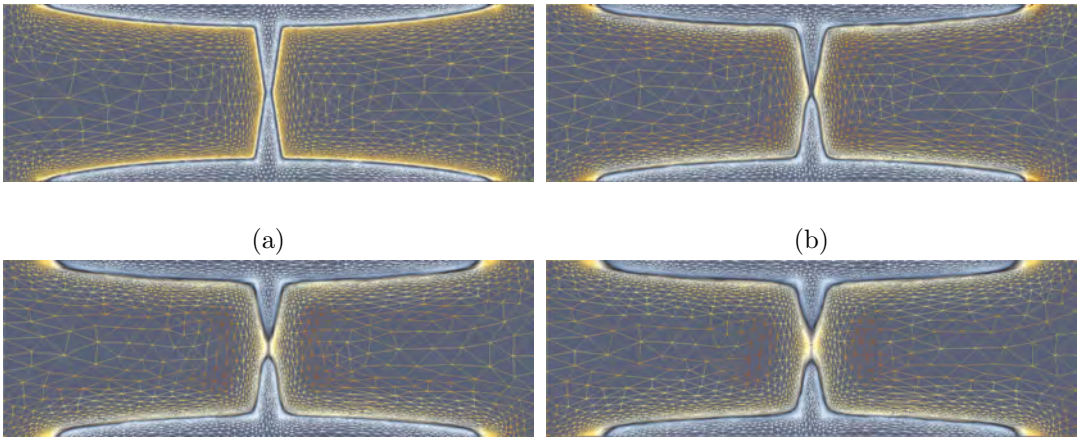

(a) (b)

(c) (d)

Figure 14: Dissolution of the conductive filament in a cation-based RRAM device: evolution of the anisotropic adapted mesh at $t = 0\,\mu s, 30\,\mu s$ (top) $t = 50\,\mu s, 100\,\mu s$ (bottom).

of CF dimension is analyzed in Sec. 8.3.
Fig. 14 illustrates the variations in CF shape during dissolution. The dissolution process works by smoothing out the sharp corners of the initial geometry, such as the constriction of the CF and the top and bottom bases of the CF. The disconnection of the CF begins from its center, namely, its thinnest part, and proceeds by causing the retraction of the CF ends towards the electrodes. The significant assistance provided by anisotropic mesh adaptation is evident. Adapted meshes allow us to model extremely thin topologies of the CF that would be impossible to identify when using a uniform mesh.

8.3 Device resistance behavior during CF growth and dissolution

In this section, we numerically investigate the correlation between RRAM cell resistance, CF shape evolution, and the applied voltage. This analysis directly considers the conductive path within the cell (for the computation of the cell resistance, we refer the reader to Appendix A).
We begin by examining the impact of the applied voltage on the formation time. The initial condition represents a scenario with a remaining CF, as shown in Fig.12 for $t = 0\,\mu s$. In left panel of Fig. 15, we provide the evolution of the device resistance during the CF growth, for three different voltage values, namely 0.75 V, 0.8 V, 0.9 V. The simulations accurately capture the expected abrupt transitions between high and low resistance states, occurring at different times depending on the applied voltage. Moreover, the model captures the well-known reduction of the switching time with the applied voltage [32, 11, 12].

As a second feature, we investigate the influence of the CF size on the relaxation time. Fig. 15, panel (b), shows the resistance evolution during dissolution for the three

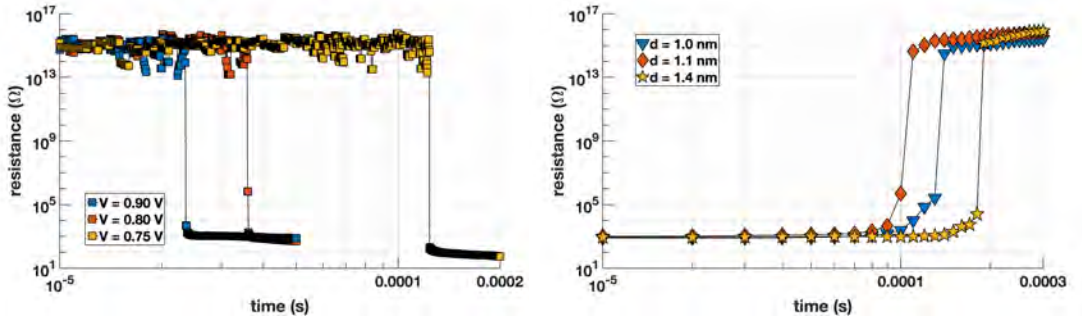

(a) (b)

Figure 15: Evolution of the resistance during CF growth (a) and dissolution (b) in a cation-based RRAM device.

initial configurations of the CF in Fig. 16. The three layouts vary in the slope of the oblique sides of the two superimposed triangles that form the CF shape, with a more vertical orientation moving from right to left. In each configuration, the minimum CF dimension d is assessed. The resistance evolution exhibits a sudden variation at different times for various initial configurations in qualitative agreement with [56].

Figure 16: Dissolution of the conductive filament in a cation-based RRAM device: different initial configurations of the CF. Each configuration is associated with a different marker.

9 Conclusions and future works

We present a novel physics-based model designed to simulate morphological changes in metallic inclusions within a dielectric exposed to an electric field. This represents a general case of nanometric conductive filaments responsible for the switching in cation-based resistive memory devices. The model takes into account both the electric-field-induced mechanisms and surface diffusion due to curvature gradient, contributing to the morphological evolution of the conductive filament simultaneously. The employment of a level-set method enhanced by an anisotropic mesh adaptation strategy and a mixed finite element formulation, enabling the simultaneous discretization of surface curvature and velocity, ensures accurate tracking of the filament shape's evolution in a computationally efficient manner, during both CF growth and dissolution of the conductive filament.
The model is numerically evaluated in a 2D framework, successfully replicating the

growth and dissolution processes of the conductive filament that govern the operation of RRAM devices.
The model also provides the capability to explore key physical quantities within the RRAM device, such as the evolution of the electric field. Furthermore, our approach can replicate the typical resistance variation over time during both growth and dissolution, emphasizing the impact of the filament's shape in these processes.

As future developments, we are planning to extensively apply the new model to simulate real electronic devices, comparing the obtained results with a diverse set of experimental data. From a modeling perspective, we will incorporate the effects induced by mechanical stress and thermal gradients.

Acknowledgments

The research work was partially supported by the European Union's Horizon 2020 Research and Innovation Program under Grant No. 871371 (MeM-Scales project), and by the CNR-IMM project 'Memristive devices for brain-inspired computing—MEMBRAIN' (DFM.AD001.265).

A Computation of the device resistance

In Fig. 15 we illustrate the device resistance behavior during the formation and dissolution of the CF. In this regard, following [56], we have generalized the methodology for calculating device resistance based on the conductivity values of the metallic material (Ag) and the dielectric oxide (SiO_x).
Let us assume that the CF is composed of a series of N_{fil} trapezoidal metallic sections, as depicted in Fig. 17. The zoom pertains to a small segment of the CF, representing a single element of the series, which is formed by two bases ($b_{1,i}$ and $b_{2,i}$) and two sides: the first one, Δy_i, is perpendicular to $b_{1,i}$ and $b_{2,i}$, while the second one is oblique, with endpoints $x_{1,i}$ and $x_{2,i}$. More precisely, Δy_i represents an edge taken along the CF axis; $b_{1,i}$ and $b_{2,i}$ denote the distances from the endpoints of Δy_i to the barycenters, $x_{1,i}$ and $x_{2,i}$, of the triangles at end of the CF itself (see the elements highlighted in red in Figure 17); the oblique side $(x_{1,i}, x_{2,i})$ is the Euclidean distance between the two barycenters.

The resistance due to the metallic area can be easily computed as follows:

$$R_{fil} = \sum_{i=1}^{N_{fil}} \frac{\rho_f |\Delta y_i|}{\pi \, |b_{i,1}| \, |b_{i,2}|}, \tag{40}$$

with $\sum_{i=1}^{N_{fil}} |\Delta y_i| = L_{CF}$ representing the CF length, and where

$$\rho_f = \rho_{f,0} \frac{1-p}{1+p} \frac{l_f}{d}$$

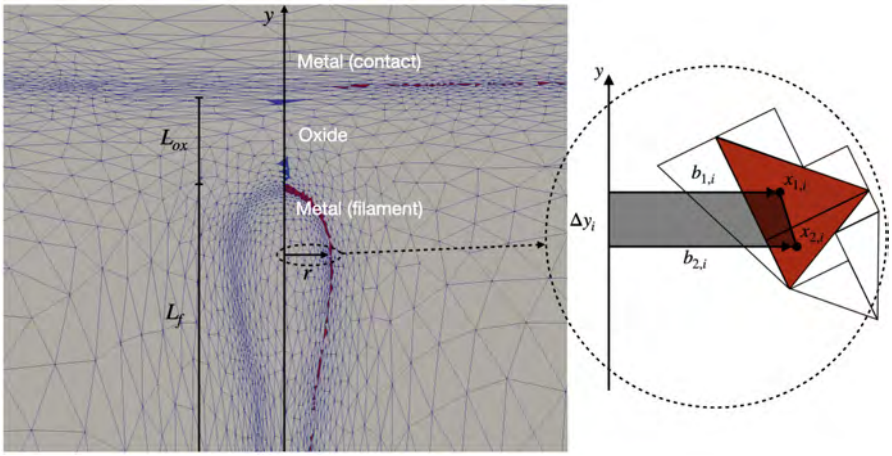

Figure 17: Numerical evaluation of the device resistance: the left panel highlights the elements identified along the metallic boundary of the CF (red elements) and the dielectric gap (blue elements); the right panel zooms in on the two elements located at the filament border.

denotes the resistivity of the metallic material [55, 54], depending on the point-by-point CF diameter, d, relative to the electron mean free path, $l_f = 53nm$. Here, $p = 0.5$ is the fraction of the electrons scattered at the CF surface, and $\rho_{f,0} = 1.59 \cdot 10^{-6}\Omega cm$, according to the nominal Ag resistivity value.

The contribution to the cell resistance from the dielectric part is computed by generalizing the approach used in [50], considering a series of N_{ox} dielectric element contributions. Let A represent the section of the conductive path in the insulator, and $\Delta y_{i,ox}$ denote the individual portion of the insulator path, such that $\sum_{i=1}^{N_{ox}} |\Delta y_{i,ox}| = L_{ox}$. The resistance due to the dielectric part can then be straightforwardly calculated as

$$R_{ox} = \sum_{i=1}^{N_{ox}} \frac{\rho_{ox}|\Delta y_{i,ox}|}{|A|}, \tag{41}$$

with $\rho_{ox} = 1 \cdot 10^{9}\Omega cm$ the resistivity of the dielectric material. Thus, we can evaluate the total device resistance by $R_{cell} = R_{fil} + R_{ox}$.

References

[1] M. Ainsworth and J.T. Oden. *A Posteriori Error Estimation in Finite Element Analysis*. John Wiley & Sons, New York, 2000.

[2] MF.A Ashby. A first report on sintering diagrams. *Acta Metallurgica et Materialia*, 22(3):275–289, 1974.

[3] M. Bernacki, Y. Chastel, T. Coupez, and RE Loge'. Level set framework for the numerical modelling of primary recrystallization in polycrystalline materials. *Scripta materialia*, 58(12):1129–1132, 2008.

[4] Andrew J Bernoff, Andrea L Bertozzi, and Thomas P Witelski. Axisymmetric surface diffusion: dynamics and stability of self-similar pinchoff. *Journal of statistical physics*, 93(3):725–776, 1998.

[5] S Brivio, S Spiga, and D Ielmini. HfO_2 -based resistive switching memory devices for neuromorphic computing. *Neuromorphic Computing and Engineering*, 2(4):042001, December 2022.

[6] Julien Bruchon, Sylvain Drapier, and François Valdivieso. 3D finite element simulation of the matter flow by surface diffusion using a level set method. *International Journal for Numerical Methods in Engineering*, 86(7):845–861, 2011.

[7] Julien Bruchon, Daniel Pino Muñoz, François Valdivieso, Sylvain Drapier, and Guillaume Pacquaut. 3D simulation of the matter transport by surface diffusion within a level-set context. *European Journal of Computational Mechanics/Revue Européenne de Mécanique Numérique*, 19(1-3):281–292, 2010.

[8] M. Burger, F. Hausser, and C. Voigt A. Stocker. A level-set approach to anisotropic flows with curvature regularization. *Journal of Computational physics*, 224(1):183–205, 2007.

[9] Milan Buttberg, Ilia Valov, and Stephan Menzel. Simulating the filament morphology in electrochemical metallization cells. *Neuromorphic Computing and Engineering*, 2023.

[10] John W Cahn and Jean E Taylor. Overview no. 113 surface motion by surface diffusion. *Acta metallurgica et materialia*, 42(4):1045–1063, 1994.

[11] Solomon Amsalu Chekol, Stephan Menzel, Rana Walied Ahmad, Rainer Waser, and Susanne Hoffmann-Eifert. Effect of the Threshold Kinetics on the Filament Relaxation Behavior of Ag-Based Diffusive Memristors. *Advanced Functional Materials*, 32(15):2111242, April 2022.

[12] Solomon Amsalu Chekol, Stephan Menzel, Rainer Waser, and Susanne Hoffmann-Eifert. Strategies to Control the Relaxation Kinetics of Ag-Based Diffusive Memristors and Implications for Device Operation. *Advanced Electronic Materials*, page 2200549, July 2022.

[13] Hong-Yu Chen, Stefano Brivio, Che-Chia Chang, Jacopo Frascaroli, Tuo-Hung Hou, Boris Hudec, Ming Liu, Hangbing Lv, Gabriel Molas, Joon Sohn, Sabina Spiga, V. Mani Teja, Elisa Vianello, and H.-S. Philip Wong. Resistive random access memory (RRAM) technology: From material, device, selector, 3D integration to bottom-up fabrication. *Journal of Electroceramics*, 39(1-4):21–38, December 2017.

[14] Davide Cortellessa, Nicola Ferro, Simona Perotto, and Stefano Micheletti. Enhancing level set-based topology optimization with anisotropic graded meshes. *Appl. Math. Comput.*, 447:Paper No. 127903, 20, 2023.

[15] Keenan Crane, Clarisse Weischedel, and Max Wardetzky. The heat method for distance computation. *Communications of the ACM*, 60(11):90–99, 2017.

[16] Sven Dirkmann and Thomas Mussenbrock. Resistive switching in memristive electrochemical metallization devices. *AIP Advances*, 7(6):065006, June 2017.

[17] Cecile Dobrzynski. MMG3D: User guide. *HAL*, 2012, 2012.

[18] Pierre Dorion, Olga Cueto, Marina Reyboz, Elisa Vianello, Jean Charles Barbé, Andreea Grigoriu, and Yvon Maday. Simulation of CBRAM devices with the level set method. In *2013 International Conference on Simulation of Semiconductor Processes and Devices (SISPAD)*, pages 340–343. IEEE, 2013.

[19] Alexandre Ern and Jean-Luc Guermond. *Theory and Practice of Finite Elements*, volume 159 of *Applied Mathematical Sciences*. Springer-Verlag, New York, 2004.

[20] PE Farrell, Stefano Micheletti, and Simona Perotto. An anisotropic Zienkiewicz–Zhu-type error estimator for 3D applications. *Internat. J. Numer. Methods Engrg.*, 85(6):671–692, 2011.

[21] Luca Formaggia and Simona Perotto. New anisotropic a priori error estimates. *Numerische Mathematik*, 89(4):641–667, 2001.

[22] P. Frey and P.-L. George. *Mesh Generation. Application to Finite Elements*. Wiley, London, second edition, 2008.

[23] Jérémy Guy, Gabriel Molas, Philippe Blaise, Mathieu Bernard, Anne Roule, Gilles Le Carval, Vincent Delaye, Alain Toffoli, Gérard Ghibaudo, Fabien Clermidy, et al. Investigation of forming, set, and data retention of conductive-bridge random-access memory for stack optimization. *IEEE Transactions on Electron Devices*, 62(11):3482–3489, 2015.

[24] W. Jost. *Diffusion in Solids, Liquids, Gases*. Academic Press, Inc, New York, 1952.

[25] Rahul B Karyappa, Shivraj D Deshmukh, and Rochish M Thaokar. Breakup of a conducting drop in a uniform electric field. *Journal of fluid mechanics*, 754:550–589, 2014.

[26] Sen Lin, Liang Zhao, Jinyu Zhang, Huaqiang Wu, Yan Wang, He Qian, and Zhiping Yu. Electrochemical simulation of filament growth and dissolution in conductive-bridging RAM (CBRAM) with cylindrical coordinates. In *2012 International Electron Devices Meeting*, pages 26–3. IEEE, 2012.

[27] A.G. Mauri, B. Morini, S. Perotto, and F. Sgallari. *Handbook of Semiconductor devices*, volume chap.38. Springer, 2023.

[28] Aurelio Giancarlo Mauri, Andrea Bortolossi, Giovanni Novielli, and Riccardo Sacco. 3d finite element modeling and simulation of industrial semiconductor devices including impact ionization. *Journal of Mathematics in Industry*, 5(1):1–18, 2015.

[29] Aurelio Giancarlo Mauri, Riccardo Sacco, and Maurizio Verri. Electro-thermochemical computational models for 3D heterogeneous semiconductor device simulation. *Applied Mathematical Modelling*, 39(14):4057–4074, 2015.

[30] Stephan Menzel, Philip Kaupmann, and Rainer Waser. Understanding filamentary growth in electrochemical metallization memory cells using kinetic Monte Carlo simulations. *Nanoscale*, 7(29):12673–12681, 2015. Publisher: Royal Society of Chemistry.

[31] Stephan Menzel, Bart Klopstra, Carsten Kügeler, Ulrich Böttger, Georgi Staikov, and Rainer Waser. A simulation model of resistive switching in electrochemical metallization memory cells (ECM). *MRS Online Proceedings Library (OPL)*, 1160:1160–H09, 2009.

[32] Stephan Menzel, Stefan Tappertzhofen, Rainer Waser, and Ilia Valov. Switching kinetics of electrochemical metallization memory cells. *Physical Chemistry Chemical Physics*, 15(18):6945–6952, 2013.

[33] Sameer Mhatre, Sébastien Simon, and Johan Sjöblom. Methodology to calculate interfacial tension under electric field using pendent drop profile analysis. *Proceedings of the Royal Society A*, 475(2225):20180852, 2019.

[34] S. Micheletti, S. Perotto, and L. Soli. Topology optimization driven by anisotropic mesh adaptation: towards a free-form design. *Computers & Structures*, 214:60–72, 2019.

[35] Stefano Micheletti and Simona Perotto. Reliability and efficiency of an anisotropic Zienkiewicz-Zhu error estimator. *Comput. Methods Appl. Mech. Engrg.*, 195(9-12):799–835, 2006.

[36] Stefano Micheletti and Simona Perotto. Anisotropic adaptation via a Zienkiewicz–Zhu error estimator for 2d elliptic problems. In *Numerical Mathematics and Advanced Applications 2009*, pages 645–653. Springer, 2010.

[37] Michael J Miksis. Shape of a drop in an electric field. *The Physics of Fluids*, 24(11):1967–1972, 1981.

[38] Lin Mu and Rabeea Jari. A recovery-based error estimate for nonconforming finite volume methods of interface problems. *Appl. Math. Comput.*, 220:63–74, 2013.

[39] William W Mullins. Theory of thermal grooving. *Journal of Applied Physics*, 28(3):333–339, 1957.

[40] Stanley Osher and James A Sethian. Fronts propagating with curvature-dependent speed: Algorithms based on hamilton-jacobi formulations. *Journal of computational physics*, 79(1):12–49, 1988.

[41] Feng Pan and Vivek Subramanian. A kinetic monte carlo study on the dynamic switching properties of electrochemical metallization RRAMs during the SET process. In *2010 International Conference on Simulation of Semiconductor Processes and Devices*, pages 19–22. IEEE, 2010.

[42] Simona Perotto and Luca Formaggia, editors. *New Challenges in Grid Generation and Adaptivity for Scientific Computing*, volume 5 of *SEMA SIMAI Springer Series*. Springer, Cham, 2015.

[43] G. M. Porta, S. Perotto, and F. Ballio. Anisotropic mesh adaptation driven by a recovery-based error estimator for shallow water flow modeling. *Internat. J. Numer. Methods Fluids*, 70(3):269–299, 2012.

[44] MN. Rahaman. *Ceramic processing and Sintering*. Marcel Dekker Inc., 1995.

[45] R. Sacco, A.G. Mauri, and G. Guidoboni. A stabilized dual mixed hybrid finite element method with lagrange multipliers for three-dimensional problems with interfaces. *Journal of Scientific Computation*, 82(60), 2020.

[46] James A Sethian and David Chopp. Motion by intrinsic laplacian of curvature. *Interfaces and Free boundaries*, 1(1):107–123, 1999.

[47] James Albert Sethian. *Level set methods and fast marching methods: evolving interfaces in computational geometry, fluid mechanics, computer vision, and materials science*, volume 3. Cambridge university press, 1999.

[48] Rubén Sevilla, Simona Perotto, and Kenneth Morgan, editors. *Mesh Generation and Adaptation-Cutting-Edge Techniques*, volume 30 of *SEMA SIMAI Springer Series*. Springer, Cham, 2022.

[49] Sabina Spiga, Abu Sebastian, Damien Querlioz, and Bipin Rajendran. *Memristive Devices for Brain-Inspired Computing*. Woodhead Publishing Series in Electronic and Optical Materials. Woodhead Publishing, 2020.

[50] F. Vaccaro, S. Brivio, S. Perotto, A.G. Mauri, and S. Spiga. Physics-based compact modelling of the analog dynamics of HfO_x resistive memories. *Neuromorphic Computing and Engineering*, 2(2):021003, jun 2022.

[51] Ilia Valov, Rainer Waser, John R. Jameson, and Michael N. Kozicki. Electrochemical metallization memories—fundamentals, applications, prospects. *Nanotechnology*, 22(25):254003, May 2011.

[52] Luis Ville, Luisa Silva, and Thierry Coupez. Convected level set method for numerical simulation of fluid buckling. *International Journal on numerical methods in engineering*, 66(3):324–344, 2011.

[53] Qiming Wang, Zhigang Suo, and Xuanhe Zhao. Bursting drops in solid dielectrics caused by high voltages. *Nature communications*, 3(1):1157, 2012.

[54] W. Wang, A. Bricalli, M. Laudato, E. Ambrosi, E. Covi, and D. Ielmini. Physics-based modeling of volatile resistive switching memory (RRAM) for crosspoint selector and neuromorphic computing. In *2018 IEEE International Electron Devices Meeting (IEDM)*, pages 40.3.1–40.3.4, San Francisco, CA, December 2018. IEEE.

[55] W. Wang, M. Laudato, E. Ambrosi, A. Bricalli, E. Covi, Y. Lin, and D. Ielmini. Volatile Resistive Switching Memory Based on Ag Ion Drift/Diffusion—Part II: Compact Modeling. *IEEE Transactions on Electron Devices*, 66(9):3802–3808, September 2019. Number: 9 Conference Name: IEEE Transactions on Electron Devices.

[56] Wei Wang, Ming Wang, Elia Ambrosi, Alessandro Bricalli, Mario Laudato, Zhong Sun, Xiaodong Chen, and Daniele Ielmini. Surface diffusion-limited lifetime of silver and copper nanofilaments in resistive switching devices. *Nature communications*, 10(1):1–9, 2019.

[57] Zhongrui Wang, Saumil Joshi, Sergey E. Savel'ev, Hao Jiang, Rivu Midya, Peng Lin, Miao Hu, Ning Ge, John Paul Strachan, Zhiyong Li, Qing Wu, Mark Barnell, Geng-Lin Li, Huolin L. Xin, R. Stanley Williams, Qiangfei Xia, and J. Joshua Yang. Memristors with diffusive dynamics as synaptic emulators for neuromorphic computing. *Nature Materials*, 16(1):101–108, January 2017. Number: 1 Publisher: Nature Publishing Group.

[58] Zhongrui Wang, Mingyi Rao, Rivu Midya, Saumil Joshi, Hao Jiang, Peng Lin, Wenhao Song, Shiva Asapu, Ye Zhuo, Can Li, Huaqiang Wu, Qiangfei Xia, and J. Joshua Yang. Threshold Switching of Ag or Cu in Dielectrics: Materials, Mechanism, and Applications. *Advanced Functional Materials*, 28(6):1704862, 2017.

[59] Rainer Waser, Regina Dittmann, Georgi Staikov, and Kristof Szot. Redox-based resistive switching memories–nanoionic mechanisms, prospects, and challenges. *Advanced materials*, 21(25-26):2632–2663, 2009.

[60] Ningning Yan. A posteriori error estimators of gradient recovery type for elliptic obstacle problems. volume 15, pages 333–362. 2001.

[61] Yuchao Yang, Peng Gao, Linze Li, Xiaoqing Pan, Stefan Tappertzhofen, Shin-Hyun Choi, Rainer Waser, Ilia Valov, and Wei D Lu. Electrochemical dynamics of nanoscale metallic inclusions in dielectrics. *Nature communications*, 5(1):4232, 2014.

[62] Mohammed A Zidan, John Paul Strachan, and Wei D Lu. The future of electronics based on memristive systems. *Nature electronics*, 1(1):22–29, 2018.

[63] Olgierd C Zienkiewicz and Jian Z Zhu. A simple error estimator and adaptive procedure for practical engineerng analysis. *International journal for numerical methods in engineering*, 24(2):337–357, 1987.

[64] Olgierd Cecil Zienkiewicz and Jian Zhong Zhu. The superconvergent patch recovery and a posteriori error estimates. part ii: Error estimatesand adaptivity. *International Journal for Numerical Methods in Engineering*, 33(7):1365–1382, 1992.

MOX Technical Reports, last issues

Dipartimento di Matematica
Politecnico di Milano, Via Bonardi 9 - 20133 Milano (Italy)

14/2024 Zappon, E.; Salvador, M.; Piersanti, R.; Regazzoni, F.; Dede', L.; Quarteroni, A.
An integrated heart-torso electromechanical model for the simulation of electrophysiogical outputs accounting for myocardial deformation

12/2024 Zingaro, A.; Ahmad, Z.; Kholmovski, E.; Sakata, K.; Dede', L.; Morris, A.K.; Quarteroni, A.; Trayanova, N.A.
A comprehensive stroke risk assessment by combining atrial computational fluid dynamics simulations and functional patient data

Antonietti, P.F.; Corti, M.
Numerical modelling of protein misfolding in neurodegenerative diseases a computational study

11/2024 Antonietti, P.F.; Corti, M.
Numerical modelling of protein misfolding in neurodegenerative diseases: a computational study

10/2024 Capuano E.; Regazzoni F.; Maines M.; Fornara S.; Locatelli V.; Catanzariti D.; Stella S.; Nobile F.; Del Greco M.; Vergara C.
Personalized Computational Electro-mechanics Simulations to Optimize Cardiac Resynchronization Therapy

09/2024 Leimer Saglio, C. B.: Pagani, S.; Corti, M.; Antonietti, P. F.
A high-order discontinuous Galerkin method for the numerical modeling of epileptic seizures

05/2024 Conti, P.; Gobat, G.; Fresca, S.; Manzoni, A.; Frangi, A.
Reduced order modeling of parametrized systems through autoencoders and SINDy approach: continuation of periodic solutions

06/2024 Antonietti, P.F., Bonetti, S., Botti, M., Corti, M., Fumagalli, I., Mazzieri, I.
lymph: discontinuous poLYtopal methods for Multi-PHysics differential problems

04/2024 Torzoni, M.; Tezzele, M.; Mariani, S.; Manzoni, A.; Willcox, K.E.
A digital twin framework for civil engineering structures

03/2024 Ciaramella, G.; Gander, M.J.; Vanzan, T.
A gentle introduction to interpolation on the Grassmann manifold